Monthly Notices of the ROYAL ASTRONOMICAL SOCIETY

MNRAS **509,** 5382–5398 (2022)
Advance Access publication 2021 November 3

https://doi.org/10.1093/mnras/stab3184

H α-based star formation rates in and around $z \sim 0.5$ EDisCS clusters

Jennifer R. Cooper,[1★] Gregory H. Rudnick,[1] Gabriel G. Brammer,[2,3] Tyler Desjardins,[4] Justin L. Mann,[1] Benjamin J. Weiner,[5] Alfonso Aragón-Salamanca,[6] Gabriella De Lucia,[7] Vandana Desai,[8] Rose A. Finn,[9] Pascale Jablonka,[10,11] Yara L. Jaffé,[12] John Moustakas,[9] Damien Spérone-Longin,[10] Harry I. Teplitz,[8] Benedetta Vulcani[13] and Dennis Zaritsky[5]

[1]*Department of Physics and Astronomy, The University of Kansas, 1251 Wescoe Hall Drive, Lawrence, KS 66045, USA*
[2]*Niels Bohr Institute, University of Copenhagen, Jagtvej 128, DK-2200 København N, Denmark*
[3]*Cosmic Dawn Center (DAWN), Jagtvej 128, DK2200 Copenhagen N, Denmark*
[4]*Space Telescope Science Institute, 3700 San Martin Dr, Baltimore, MD 21218, USA*
[5]*Steward Observatory, University of Arizona, 933 North Cherry Avenue, Tucson, AZ 85721, USA*
[6]*School of Physics and Astronomy, University of Nottingham, University Park, Nottingham NG7 2RD, UK*
[7]*INAF - Osservatorio Astronomico di Trieste, via G. B. Tiepolo 11, I-34143 Trieste, Italy*
[8]*Infrared Processing and Analysis Center, California Institute of Technology, MS 100-22, Pasadena, CA 91125, USA*
[9]*Siena College, 515 Loudon Rd., Loudonville, NY 12211, USA*
[10]*Institute of Physics, Laboratory of Astrophysics, École Polytechnique Fédérale de Lausanne (EPFL), CH-1290 Sauverny, Switzerland*
[11]*GEPI, Observatoire de Paris, Université PSL, aNRS, Place Jules Janssen, F-92190 Meudon, France*
[12]*Instituto de Física y Astronomía, Universidad de Valparaíso, Avda. Gran Bretaña 1111 Valapraíso, Chile*
[13]*INAF – Osservatorio Astronomico di Padova, Vicolo Osservatorio 5, I-35122 Padova, Italy*

Accepted 2021 October 26. Received 2021 October 21; in original form 2021 March 1

ABSTRACT

We investigate the role of environment on star formation rates (SFRs) of galaxies at various cosmic densities in well-studied clusters. We present the star-forming main sequence for 163 galaxies in four EDisCS clusters in the range $0.4 < z < 0.7$. We use *Hubble Space Telescope*/Wide Field Camera 3 observations of the H α emission line to span three distinct local environments: the cluster core, infall region, and external field galaxies. The main sequence defined from our observations is consistent with other published H α distributions at similar redshifts but differs from those derived from star formation tracers such as 24 μm. We find that the Hα-derived SFRs for the 67 galaxies with stellar masses greater than the mass-completeness limit of $M_* > 10^{9.75}\,\mathrm{M}_\odot$ show little dependence on environment. At face value, the similarities in the SFR distributions in the three environments may indicate that the process of finally shutting down star formation is rapid, however, the depth of our data and size of our sample make it difficult to conclusively test this scenario. Despite having significant H α emission, 21 galaxies are classified as *UVJ*-quiescent and may represent a demonstration of the quenching of star formation caught in the act.

Key words: galaxies: clusters: general – galaxies: evolution – galaxies: star formation.

1 INTRODUCTION

Star formation governs the conversion of a galaxy's gas into stars and is characterized by the balance of cold gas accretion and feedback (Bouché et al. 2010; Dutton et al. 2010). Global star formation peaked at $z \sim 2$ and has been in a rapid decline to the present day (Cucciati et al. 2012; Madau & Dickinson 2014; Bouwens et al. 2015). Across all redshifts and masses, a tight correlation illustrates that more massive star-forming galaxies are forming stars at a quicker rate than those at lower stellar masses; this relation is referred to as the star-forming main sequence (Noeske et al. 2007; Peng et al. 2010; Whitaker et al. 2012). The normalization of the star-forming main sequence evolves with time, where galaxies at $z \sim 2$ and $z \sim 1$ have a main sequence that is 20× (Daddi et al. 2007) and 7× higher (Elbaz et al. 2007), respectively, than at $z \sim 0$ (Brinchmann et al. 2004). This decline in overall star formation to the present day poses many questions surrounding the nature and fate of the Universe.

While the main sequence is generally presented with a slope ranging from 0.2 to 1.2 (Speagle et al. 2014), there have been numerous studies that show that bulge-dominated massive galaxies contribute towards a flattening in the star formation rate (SFR) at higher masses (Karim et al. 2011; Whitaker et al. 2012, 2014; Schreiber et al. 2015; Erfanianfar et al. 2016). This 'internal' quenching mechanism is directly related to the morphology of the galaxy and results in a less efficient conversion of gas to stars (Martig et al. 2009). Processes that suppress star formation, such as expulsion of the gas through feedback, a cutoff in gas accretion (Larson, Tinsley & Caldwell 1980), or the removal of the gas via ram-pressure stripping (Quilis, Moore & Bower 2000), can also cause a deviation to SFRs lower than the main sequence. Additionally, some ram-pressure stripping and merger events have been observed to first create enhanced SFR activity, followed by a suppression phase (Jaffé et al. 2016; Poggianti et al. 2016; Vulcani et al. 2018). The overall observed scatter in the

★ E-mail: jrc323@cornell.edu

main sequence is likely due to varying star formation histories of each galaxy (Domínguez Sánchez et al. 2014; Hopkins et al. 2014), where this scatter is consistent across stellar mass and redshift at ∼ 0.3 dex (Whitaker et al. 2012; Tacchella et al. 2016).

Further exploration of the SFR–stellar mass relation is expanded by investigating distinct cosmic environments. The densest regions of the Universe consist of galaxy clusters with thousands of members that are gravitationally bound and contain a hot intracluster medium (ICM). Many of the most massive galaxies reside in the cluster cores, with the brightest cluster galaxy (BCG) generally being at the minimum or centre of the cluster potential well and elliptical in shape. However, cluster membership extends far beyond the virial radius and encompasses the infall region where galaxies are initially accreted into the cluster environment. This infall region of galaxy clusters has the potential to host the sites of galaxy transformation and quenching processes *in situ* that may differ from those in the core. Just et al. (2019) found that 30–70 per cent of the galaxies in local clusters were located in the infall region at $z \sim 0.6$, meaning that these galaxies may become the majority of cluster galaxies at $z \sim 0$. This finding reinforces the importance of the cluster infall region with respect to the environmentally driven transformation of galaxies.

There have been numerous studies of star formation in clusters, conducted using various emission lines. Studies which consider the galaxy population as a whole see a clear suppression of star formation in dense environments (e.g. Balogh et al. 1997; Kauffmann et al. 2004; Patel et al. 2009). It is now recognized that this difference is primarily driven by the higher fraction of passive galaxies in clusters compared to the field. When considering only star-forming galaxies, studies yield conflicting pictures as to the effect of galaxy environment on the SFR of star-forming galaxies. For example, various authors find no difference in the SFRs of star-forming galaxies in low- and high-density environments (e.g. Poggianti et al. 2008; Peng et al. 2010; Koyama et al. 2013; Tiley et al. 2020). However, other studies find evidence for a suppression of star formation in cluster galaxies relative to the field, mostly manifested in a tail to low SFRs (Wolf et al. 2009; Finn et al. 2010; Vulcani et al. 2010; Paccagnella et al. 2016; Old et al. 2020). These studies indicate that the cluster environment is indeed suppressing SFRs of star-forming galaxies, though perhaps only for a subset of the population. The apparent contradiction between these studies is somewhat difficult to reconcile for multiple reasons. The studies use various tracers, have different sensitivities to low SFR, and do not all probe the same dynamic range in density. However, most modern studies that examine clusters and are sensitive to low SFRs do find an excess population in clusters with suppressed star formation (e.g. Paccagnella et al. 2016). These results indicate that star formation is being quenched in clusters. The time-scale needed to quench star formation is highly dependent on the exact distribution of SFRs below the main sequence. For example, a lack of galaxies below the main sequence would argue for a fast quenching time-scale (<1 Gyr). This is necessary to avoid a substantial population of galaxies with significantly reduced but non-zero SFRs.

In contrast to this fast time-scale, studies which model the buildup of quiescent galaxies in clusters over time require a significantly longer time-scale between when galaxies cross the virial radius and when they quench, of the order of five Gyr at $z \sim 0$ and shorter at higher redshift (McGee et al. 2011; De Lucia et al. 2012; Muzzin et al. 2014; Taranu et al. 2014; Haines et al. 2015; Fossati et al. 2017). A proposal for reconciling these different time-scale is one in which galaxies follow a delayed-then-rapid quenching process as they fall into a more massive halo (Wetzel et al. 2013). In this picture, galaxy SFRs are unaffected for the first 2–4 Gyr (Wetzel et al. 2013), followed by a rapid quenching period. This proposal has been remarkably successful at explaining both the evolution in the quenched fraction and the distribution of galaxy SFRs. Despite this success, the physical processes acting during the 'delay' phase, and the process responsible for the ultimate 'rapid' quenching remain ambiguous. Indeed, some recent studies indicate that this phase is one in which the spatial extent of the star formation within star-forming cluster galaxies is being slowly reduced, thus indicating that the 'delay' phase is really a slow quenching phase (Finn et al. 2018).

Making progress in our understanding of galaxy quenching in dense environments requires studies that probe the distribution of SFRs for star-forming galaxies to low levels of SFR and over a large dynamic range in densities and with a single tracer. It is also important that studies extend beyond the local Universe, as quenching time-scales evolved to longer times at lower redshift (Balogh et al. 2016; Foltz et al. 2018). To probe the full evolution of galaxy SFRs as galaxies fall into clusters, a final ingredient is that studies probe beyond the virial radius into the infall regions, as that is where environmental transformation may first occur (Lewis et al. 2002; Gómez et al. 2003). H α is an excellent tracer of star formation as it is less susceptible to extinction or metallicity than other optical emission lines, such as [O II] (e.g. Moustakas, Kennicutt & Tremonti 2006), and because it probes the instantaneous SFR (Kennicutt 1998). There have been a small number of wide-field H α studies of clusters beyond the local Universe (Kodama et al. 2004; Koyama et al. 2011; Sobral et al. 2011). These have focused on very massive clusters and have included only one cluster per study. However, they do not present a consistent picture of the effect of the infall region. For example, Koyama et al. (2011) find that the fraction of H α emitters with red colours peaks in groups but is elevated in groups in the infall region with respect to the core. On the other hand, Sobral et al. (2011) find that the SFR of H α emitters climbs significantly from low to intermediate densities but declines again at the highest densities that correspond to cluster cores. However, Sobral et al. (2011) also find that this boosting of the SFR is dominated by galaxies with stellar masses lower than $10^{10.6}\,\mathrm{M}_{\odot}$. These varied results highlight the need for studies of the SFR in the infall regions of multiple clusters with the same tracer and survey selection. Having larger samples of clusters is especially important given the significant cluster-to-cluster variation in galaxy properties (e.g. Poggianti et al. 2006; Moran et al. 2007; Patel et al. 2011; Oemler et al. 2013).

At $z \gtrsim 0.5$, the H α line is located at $\lambda_{\rm obs} > 1.0\,\mu$m which is difficult to observe from the ground. The *Hubble Space Telescope* (*HST*) provides access to H α through slitless spectroscopy using The Wide Field Camera 3 (WFC3). The 3DHST survey (van Dokkum et al. 2011; Momcheva et al. 2016) demonstrated the power of this mode by observing more than 100 000 galaxies in the CANDELS fields. The grism spectra, coupled with broad-band imaging, allowed the 3DHST team to produce and release robust redshifts, emission-line fluxes, and 2D emission- line spatial maps. This showcased the power of the grism and led to numerous publications regarding sizes (Nelson et al. 2012; van der Wel et al. 2014), the main sequence (Whitaker et al. 2012, 2014), and assembly of galaxies (van Dokkum et al. 2013; Barro et al. 2014; Lang et al. 2014). The success of this study led to other surveys utilizing the same combination of observation modes such as the Grism Lens-Amplified Survey from Space (GLASS; Treu et al. 2015), which was able to observe galaxies in varying cosmic environments (Vulcani et al. 2015, 2016, 2017; Abramson et al. 2018). GLASS and other surveys (Lotz et al. 2013; Lee-Brown et al. 2017) demonstrated the abilities of the *HST* grism even in crowded cosmic regions.

This study aims to characterize the distribution of SFRs in galaxies in the infall and core regions of four $z \sim 0.5$ clusters, and to compare them to a consistently measured field sample. We seek to quantify how SFRs are affected during a galaxy's journey into the cluster environment. This paper is organized as follows. In Section 2, we describe the sample properties, observations, and reduction methodologies. In Sections 3 and 4, we present the SFR–stellar mass results and comparison to the literature. In Section 5, we discuss future work and analysis possible with this data set. The virial radius (R_{200}) is defined as the radius of the enclosed circle that has a density, ρ, 200× that of the critical density, ρ_c, of the Universe at a given redshift. All magnitudes are given in the AB system, and we assume a Chabrier initial mass function (Chabrier 2003). We adopt a Lambda cold dark matter cosmology with $\Omega_m = 0.307$, $\Omega_\Lambda = 0.693$, and $H_0 = 67.7$ km s^{-1} Mpc^{-1} (Planck Collaboration XIII 2016).

2 METHODOLOGY AND DATA

2.1 ESO distant cluster survey

The ESO Distant Cluster Survey (EDisCS; White et al. 2005) is an ESO Large Program derived from the optically brightest objects of the Las Campañas Distant Cluster Survey (Gonzalez et al. 2001) and comprises 20 clusters within $0.4 < z < 0.8$. The velocity dispersion (σ_v) of these clusters ranges from 200 to 1200 km s^{-1} (Halliday et al. 2004; Milvang-Jensen et al. 2008) and is characteristic of local cluster progenitors due to mid-mass halo sizes (Milvang-Jensen et al. 2008). The main goal of EDisCS is to examine the evolution of cluster populations over a large span of cosmic time and compare results to with respect to halo mass and local cluster populations.

For the purpose of this study, we decide to separate our galaxies into three distinct, but broadly defined, environments: (i) the cluster core, within R_{200}, (ii) the infall region, which corresponds to all galaxies at the cluster redshift but beyond the virial radius, and (iii) the field, which corresponds to foreground and background galaxies. We define the cluster centre in all cases as the location of the BCG and measure clustercentric radii from that location. The BCG lies at the approximate centre of the member distribution (White et al. 2005) for our clusters and Just et al. (2019) showed that any offsets of the BCG location from the centre are < 10 per cent of the infall radius for the clusters in our sample. However, some of our clusters exhibit significant substructure (De Lucia et al. 2009), indicating that defining environment purely by clustercentric radius may wash out some trends with local density.

2.1.1 Cluster core

The core regions, which are typically of the order of 0.5–2 Mpc across, are defined as the area within the virial radius and typically include the BCG. For EDisCS, the cores have been extensively studied with deep optical imaging and spectroscopy on VLT (Halliday et al. 2004; White et al. 2005; Milvang-Jensen et al. 2008; Vulcani et al. 2012) and near-infrared (IR) observations on the New Technology Telescope (White et al. 2005; Rudnick et al. 2009) which has allowed further EDisCS studies such as brightest cluster galaxy identification (White et al. 2005; Whiley et al. 2008), morphologies (Desai et al. 2007; Simard et al. 2009; Vulcani et al. 2011b, a), fundamental-plane parameters (Saglia et al. 2010), red-sequence identification (De Lucia et al. 2004), weak lensing (Clowe et al. 2006), 24 μm MIPS SFRs (Finn et al. 2010), and [O II] SFRs (Poggianti et al. 2006, 2009; Vulcani et al. 2010). Cluster cores are dense regions that are attractive for studying cluster properties and are well-suited for observations due to high contrast with the background and density of objects within a given field of view (FOV). However, physical processes affecting the evolution of a galaxy appear to occur as these sources enter a cluster environment, and thus the cores likely only provide information on their fate. This is reinforced through observations that the cores typically include a higher fraction of massive red disc or quiescent galaxies (Dressler 1980; Bell et al. 2004; Kauffmann et al. 2004; Erfanianfar et al. 2016). A spatially expanded view of clusters is required to gather information on environmentally driven quenching mechanisms across a representative sample of galaxies within a cluster.

2.1.2 Wide-field follow-up surveys

Galaxy clusters extend far beyond their cores and virial radii, and in order to achieve a more informed understanding of the role of environment on galaxy evolution, it is important to extend analyses to projected radii greater than R_{200}. This is a challenging task, as the reduced density of the cluster density profile results in a decreased contrast with the foreground and background (Newman et al. 2013), so large and wide-field spectroscopic studies are required to conclusively establish membership in these regions.

For this reason, we undertook a wide-field imaging and spectroscopic follow-up of the EDisCS clusters. The imaging consisted of *BVRIzK* data covering approximately 30 arcmin × 30 arcmin around the cluster. The *VRI* photometry was observed with the Wide Field Imager (WFI) on the 2.2-m Max Planck Gesellschaft/European Southern Observatory (MPG/ESO) telescope (Baade et al. 1999), while *Bz* observations were completed on the MOSAIC instrument on the Cerro Tololo Inter-American Observatory (CTIO) Blanco or Mayall 4-m telescope. The *K*-band data were taken with the NEWFIRM instrument on the Mayall telescope. These imaging observations are described in detail in Just et al. (2019) and Mann et al. (in preparation). The spectroscopic component of the survey was conducted with the Low-Dispersion Prism (LDP) on IMACS/Magellan, which covers out to $6R_{200}$ for our clusters. These observations produced a deep catalogue of 25 000 redshifts with an accuracy of $\sigma = 0.007$ and a high spectroscopic completeness up to $R_{\rm AUTO} < 23.3$ (Just et al. 2019). This information is crucial towards establishing cluster membership beyond the central core as in previous EDisCS studies and allows for targeted follow-up observations of groups or infalling populations.

As described in Just et al. (2019), we derived rest-frame $U - V$ and $V - J$ (hereafter *UVJ*) colours for all of our galaxies. Due to residual zero-point calibration issues, these colours required secondary adjustments to bring them in line with the *UVJ* colours as measured for core galaxies from the EDisCS survey. This process is described in Appendix A. Following those adjustments, we have reliable *UVJ* colours that can be used to separate galaxies into quiescent and star-forming (e.g. Wuyts et al. 2007; Williams et al. 2009). However, the way in which we performed the adjustments impacted the reliability of our *U*-through-*K* SEDs and added an unacceptable level of systematic uncertainty to SED-based stellar mass estimates. In Section 2.6, we describe our alternate method for our computation of the stellar mass using just the calibrated *UVJ* colours.

Just et al. (2019) utilized the theory of secondary infall to identify the infall region of the galaxy clusters with the equations given in White & Zaritsky (1992). This theory describes how shells of mass evolve with redshift when centred on a cosmic perturbation; shells

Table 1. Parameters for each of the clusters in this study from Just et al. (2019). (1) EDisCS Cluster ID (2) Right ascension in hours (3) Declination in degrees (4) Cluster redshift (5) Virial radius in Mpc (6) Infall radius in Mpc (7) Virial mass (8) Velocity dispersion. The range in velocity dispersions between the clusters is small in order to reduce cluster to cluster variation. Each of the clusters has an infall radius between 3 and 4 Mpc from the BCG-defined centre. The multiband wide-field observations in each cluster extend past the infall region for sufficient cluster coverage (Just et al. 2019).

Cluster ID (1)	RA (h) (2)	Dec. (deg) (3)	z_{spec} (4)	R_{200} (Mpc) (5)	R_{infall} (Mpc) (6)	M_{200} (10^{14} $M_\odot$) (7)	σ_v (km s^{-1}) (8)
Cl1059.2-1253	10:59:07.1	−12:53:15	0.4564	$0.99^{+0.10}_{-0.11}$	3.19	$1.78^{+0.60}_{-0.53}$	510^{+52}_{-56}
Cl1138.2-1133	11:38:10.3	−11:33:38	0.4796	$1.40^{+0.14}_{-0.15}$	4.62	$5.20^{+1.69}_{-1.46}$	732^{+72}_{-76}
Cl1227.9-1138	12:27:58.9	−11:35:13	0.6357	$1.00^{+0.13}_{-0.13}$	3.76	$2.29^{+0.97}_{-0.78}$	574^{+72}_{-75}
Cl1301.7-1139	13:01:40.1	−11:39:23	0.4828	$1.31^{+0.16}_{-0.16}$	4.34	$4.29^{+1.73}_{-1.42}$	687^{+82}_{-89}

that are contained within a critical mass will eventually follow a gravitational collapse and become bound. The outermost boundary of the mass shell that experiences collapse at the cluster redshift is defined as the infall radius.

Follow-up observations with *HST* were possible due to the extensive spectroscopic and photometric coverage of the EDisCS sample in Just et al. (2019) and the proven abilities of the grism with 3DHST (Momcheva et al. 2016) and GLASS in dense cluster environments (Treu et al. 2015). From the full EDisCS sample of 17 EDisCS clusters, we selected four clusters for follow-up with the *HST*/WFC3 G102 IR grism to produce high-spatial resolution emission-line maps for individual galaxies (Table 1). These clusters were chosen according to the following criteria: (1) The ability of *HST* to observe H α with the G102 at the redshift of the cluster and (2) the degree to which the infall region of the cluster was populated with groups at a range of clustercentric radii and with enough galaxies in each group so as to maximize the multiplexing efficiency for the grism observations.

These clusters have a velocity dispersion ranging from 500 to 800 km s^{-1}, which is squarely in the middle of the velocity dispersion range of EDisCS clusters (Halliday et al. 2004; Milvang-Jensen et al. 2008). The limited range in velocity dispersion of our target clusters will help to minimize the halo-mass dependent cluster-to-cluster variations (Poggianti et al. 2006; Moran et al. 2007). Just et al. (2019) performed a characterization of the infall region of the EDisCS clusters using the LDP spectroscopy, which showed that red galaxies are more clustered than blue galaxies. Because of the magnitude limited density-dependent sparse spectroscopic target sampling, the limited number of galaxies in each cluster's infall region, and because of the aggressive masking of bright stars in the targeting (Fig. 1), it is significantly more difficult to characterize local densities in the infall region and to identify other structures, like filaments. Details for each pointing including cluster membership and location are listed in Table 2.

2.2 Field sample

In order to form a comparison set of galaxies in an effort to constrain environmental effects from the cosmic web, we establish a field sample that is assumed to occupy a less dense and interactive region of the Universe. Nearly three-fourths of all galaxies in the Universe reside in the field and have been the subject of many surveys such as 3DHST (Momcheva et al. 2016) and CANDELS (Grogin et al. 2011). However, no large H α field sample with significant ancillary data exists at the redshift of our clusters, so we therefore construct a field sample from our own data. In our study, we construct the field using *HST*-observed galaxies within each pointing FOV in the range of $0.4 < z < 0.7$ that lie outside ± 0.02 of each cluster redshift. This span in redshift is dictated by the range of our four target clusters.

2.3 *HST*/WFC3 observations

We obtained *HST*/Wide Field Camera 3 *F*105*W* imaging and G102 grism spectroscopy in a Cycle 20 program (GO-12945: PI Rudnick) for four EDisCS clusters at $z \sim 0.5$ to target star-forming H α emitters. Details for each cluster in this study are listed in Table 1.

There are 14 pointings consisting of two orbits each (2800 s) that are distributed over the four clusters, where ∼15 per cent of the time is devoted to *F*105*W* (rest-frame *R* band) direct imaging and the remaining 85 per cent used for G102 grism spectroscopy. This is a similar split between modes as in 3DHST (Nelson et al. 2012; Momcheva et al. 2016). The distribution of the pointings aims to equally cover the cluster core and infalling region in each cluster in order to sample a range of environments, as shown in Fig. 1. The infall region pointings were chosen based on a preliminary LDP catalogue to contain projected overdensities of blue galaxies spectroscopically confirmed to lie at the cluster redshift. The LDP catalogue underwent significant revisions following the original targeting and some of the originally chosen projected groups reduced their density contrast. Of the 14 pointings, only 12 are utilized due to unreliable photometry in Cl1059; this results in the loss of two infall pointings, which are designated as dashes in Fig. 1. There are a total of 581 galaxies with LDP redshifts in these 12 pointings, which will be further reduced based on H α detection.

The G102 grism spans a wavelength range of 0.7–1.1 μm, which contains the H α emission for $0.4 < z < 0.7$. As the brightest Balmer series emission line, the H α flux can straightforwardly be transformed into an SFR (see Section 2.5 for a further explanation) and is an excellent tracer of nearly instantaneous star formation on ∼10 million year time-scales, despite having typical attenuation of 1–2 mag.

The G102 grism resolution of 700 km s^{-1} is much higher than the typical internal galaxy velocity dispersion, which results in a resolved H α map of the galaxy. The emission-line map is produced by subtracting a polynomial fit to the background from the 2D spectrum, where the emission line is initially masked. The residual provides an image of the galaxy at a given wavelength within the grism range for the masked emission line. An example of $z \sim 1$ H α emission-line maps are available from 3DHST observations in Nelson et al. (2012). Additionally, as a robust optical tracer, H α can detect SFR to low surface brightness levels, which is crucial for creating a sample that encompasses galaxies as they are shutting

Table 2. Information for each of the 14 pointings observed with *HST*/WFC3. In column 1, the prefix of the Pointing ID relates to the Cluster ID from Table 1 column 1. Columns 2 and 3 contain the RA/Dec-. information. For the Location column, I and C refer to *infall* and *core*, respectively, where *infall* is outside of R_{200} as specified in Table 1 column 6. The number of sources extracted with GRIZLI in each pointing are listed in column 5. The number of galaxies with H α S/N > 3 and without contamination in the cluster (6) and field (7) for each pointing, where H α S/N < 3 are designated within parentheses. An x signifies that the pointing was not utilized. All of these sources have a wide-field catalogue counterpart with rest-frame colours and stellar mass calculations. For Cl1059, the two pointings (12.2 and 12.3) in the core do not have well-calibrated photometric wide-field data and thus replacement observations and redshifts are utilized from previous VLT/FORS observations (White et al. 2005). The two infall pointings (Cl1059-12.0 and Cl1059-12.1) do not have substitute coverage and are not included in analysis.

Pointing ID (1)	RA (h) (2)	Dec. (deg) (3)	Location (cluster/infall) (4)	$N_{galaxies}$ (5)	$N_{cluster}$ (H α) (6)	N_{field} (H α) (7)
Cl1059-12.0	10:59:08.16	−12:45:05.04	I	161	x	x
Cl1059-12.1	10:59:03.36	−12:51:59.04	I	152	x	x
Cl1059-12.2	10:59:14.16	−12:53:11.04	C	152	8(4)	15
Cl1059-12.3	10:59:32.16	−12:54:12.64	C	179	17(2)	12
Cl1138-11.0	11:38:16.56	−11:33:23.04	C	80	15(6)	13(24)
Cl1138-11.1	11:38:51.60	−11:33:30.24	I	108	4	5(4)
Cl1138-11.2	11:37:54.48	−11:30:23.04	I	179	3(1)	7
Cl1227-11.0	12:28:02.40	−11:35:11.04	C	117	3(4)	3(2)
Cl1227-11.1	12:28:08.16	−11:31:02.64	I	167	3	5(3)
Cl1227-11.2	12:28:20.64	−11:30:59.04	I	129	3	9(3)
Cl1301-11.0	13:01:35.76	−11:36:59.04	C	167	4(3)	3(6)
Cl1301-11.1	13:01:25.44	−11:31:42.24	I	143	6(3)	6(1)
Cl1301-11.2	13:01:33.36	−11:40:27.84	C	184	5(7)	1(5)
Cl1301-11.3	13:01:02.88	−11:30:15.84	I	145	4	7(5)

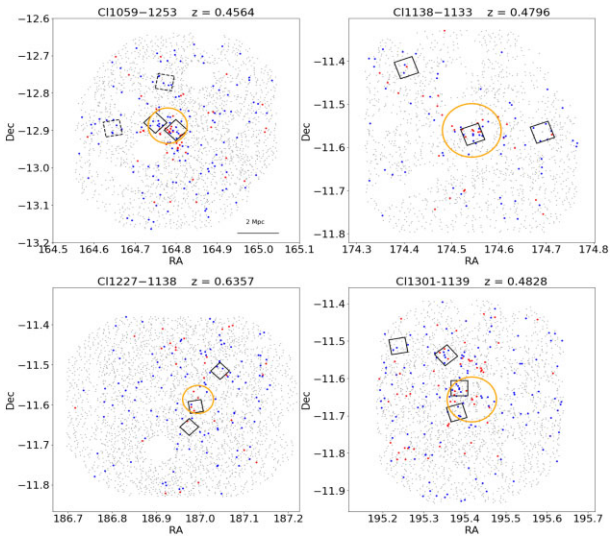

Figure 1. The RA and Dec. spatial distribution of galaxies in each cluster. Grey dots represent all galaxies in the FOV that have an LDP redshift, red/blue points signify *UVJ*-identified quiescent/star-forming cluster member sources, and the virial radius is indicated by the orange circle. No magnitude or mass limits are taken into account.
HST/WFC3 G102 observations are represented by the black squares, where the two unused infall pointings in Cl1059 are dashed. The distributed sampling among the core and infall region allows for a direct comparison of SFRs by environment.

off star formation. The SFR detection limit is variable depending on the extent and morphology of the galaxy, which makes defining a detection limit non-trivial. The lowest log(SFR) derived in this study are ~ -0.5 $M_{\odot}$ yr^{-1}, which is considered a typical value for a regular star-forming galaxy at masses similar to our target galaxies.

2.4 Data reduction

GRIZLI (grism redshift and line analysis software for space-based slitless spectroscopy)[1] is a reduction and extraction pipeline in PYTHON that allows for end-to-end processing of WFC3 data, starting from a query of the ESA Hubble Science archive to download all of the data associated with an observation ID. It then performs a routine calibration of the data, including image background sky subtraction, alignment, and flat-fielding, resulting in the two drizzled mosaic data products shown in Fig. 2. The WFC3 camera captures both an IR 1.05 μm direct image ($F105W$) and the spectrum as a dispersed image for each object in the FOV (G102 grism). The 2D spectra are the streaks, which represent the flux of each object as it is spread out over the range (0.7–1.1 μm) of the grism. Several conditions may make a grism spectrum unusable, including contamination from a bright source, low signal-to-noise ratio, or FOV restrictions. All sources included in our analysis are visually inspected for artefacts or poor modelling. While the analysis focuses on galaxies with S/N H α > 3, those with <3 are presented as down arrows in several figures.

2.5 H α line extraction and redshift prior

The redshifts in GRIZLI are fit using a coarse grid (resolution ∼0.005) with three line complex templates composed of (1) [O II] + [Ne III], (2) [O III] + H β, and (3) H α + [S II] + weaker red lines. Each of the line complexes has fixed line ratios in order to reduce line misidentification and break redshift degeneracies. A minima in the χ-squared fit on the redshift grid allows for the best-fitting determination of the redshift.

[1] GRIZLI is written and developed by Gabriel Brammer and is publicly available as open-source software: github.com/gbrammer/grizli.

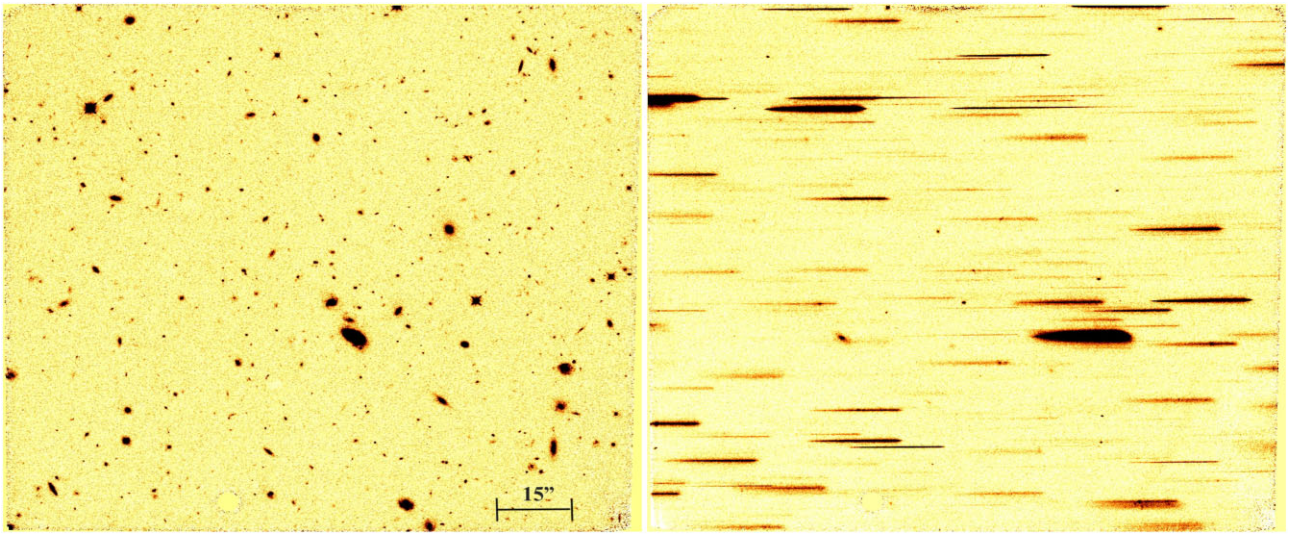

Figure 2. (Left) *HST* WFC3 *F*105*W* (1.05 μm) IR direct image of the CL1301-11.2 pointing. (Right) *HST* WFC3 G102 grism data, which provides a spatially resolved spectrum for every object in the FOV of the *F*105*W* image. The spectrum for each object is extracted within the grism wavelength range after a polynomial fit to the continuum is subtracted off.

To reduce the misidentification of other emission lines as Hα, a redshift prior is utilized during extraction within GRIZLI. Priors are derived from the LDP spectroscopic or the wide-field photometric redshift surveys. To determine the probability distribution ($P(z)$) in equation (1),

$$P(z) = \left(\sigma\sqrt{2\pi}\right)^{-1} \mathrm{e}^{\frac{-(z-z_{\mathrm{prior}})^2}{2\sigma_z^2}}, \tag{1}$$

the prior is multiplied by the GRILZI redshift fit, using either a Gaussian probability (Just et al. 2019) with a $\sigma = 0.007$ or the average of the 68 per cent photometric redshift confidence levels, respectively. Fig. 3 is a demonstration of applying the prior to a low S/N Hα galaxy that changes the determined redshift by >0.2, which is significant when cluster membership is determined within a 0.02 range in z.

A full set of data products for a strong Hα emission line Cl1059 cluster member is shown in Fig. 4. This galaxy has a spectroscopic prior applied but it also had a well-determined redshift based solely on the blind GRIZLI extraction. A comparison between the available redshifts for each galaxy in this sample with and without priors is shown in Fig. 5. The general agreement of GRIZLI z extractions without a prior to the wide-field catalogue of spectroscopic and photometric redshifts supports the usage of this software in Hα line identification without previous information, but it is most important for low S/N emission lines or quiescent galaxies where a prominent emission line may not exist. These lower S/N sources are critical for encompassing a range of SFRs in a main-sequence analysis and exclusion of these galaxies would introduce a bias towards strong emission-line galaxies.

This data set has three types of redshifts available: GRIZLI, GRIZLI + Gaussian prior from a spectroscopic LDP, and GRIZLI + Gaussian prior from a photometric wide field, where the prior is described in equation (1). GRIZLI is first run without any priors, and is then rerun to include a prior with either a spectroscopic LDP or photometric wide-field redshift for each galaxy. When compared for sources with Hα S/N > 3, the blind GRIZLI redshifts do remarkably well, with ∼85 per cent matching the extracted redshift with an LDP prior and ∼62 per cent for the photometric prior as shown in Fig. 5.

2.6 Stellar masses and star formation rate corrections

As described in Section 2.1.2 and Appendix A, due to the calibration issues with our photometry we cannot derive stellar masses for our sample using SED fitting techniques. However, we have calibrated our rest-frame *UVJ* colours by comparing them to the valid colours from the EDisCS survey. We therefore determine our stellar masses using the relation between rest-frame $U - V$ colour and V-band stellar mass-to-light ratio that is derived from continuous star formation history (SFH) models with a variety of Calzetti et al. (2000) attenuation laws. This approach is similar to that used by various authors (e.g. Bell & de Jong 2001; Vulcani et al. 2010; Taylor et al. 2011) and is primarily valid for galaxies with continuous SFHs. The derivation of our specific relation is provided in Mann et al. (in preparation) The relation we adopt is

$$\log_{10} M_* = 0.997 \times (U - V) - 1.272 + \log_{10} L_V, \tag{2}$$

where

$$\frac{L_V}{\mathrm{L}_{\odot,\mathrm{V}}} = \frac{4\pi\, f_V\, D_L^2}{(1+z)} \frac{1}{\mathrm{L}_{\odot,V}} \tag{3}$$

and f_V is the flux through the redshifted rest-frame V-band filter, D_L is the distance luminosity, and $\mathrm{L}_{\odot V}$ is the rest-frame luminosity of the sun in V band. Stellar masses determined from a single colour can have systematic errors of the order of 0.3 dex stemming from variations in the dust attenuation, metallicity, and SFH. In addition, we applied systematic corrections of less than 0.2 mag to our $U - V$ colours that may also be uncertain and can result in additional stellar mass errors up to 0.2 dex. We therefore conservatively assume stellar mass uncertainties up to 0.5 dex, with the consideration that the statistical uncertainties on photometric measurements are significantly less than this, especially for the bright galaxies with LDP redshifts, and can be ignored.

The mass-completeness level is independently identified at this value through (1) a comparison of the stellar masses of the 163 *HST*-observed galaxies to the ULTRAVISTA star-forming subset at a similar redshift range and (2) by the 2σ distribution of all star-forming galaxies in the EDisCS sample from Just et al. (2019) within the photometric completeness limit and redshift range. This results in a mass-complete value of $10^{9.75}\ M_*/\mathrm{M}_\odot$.

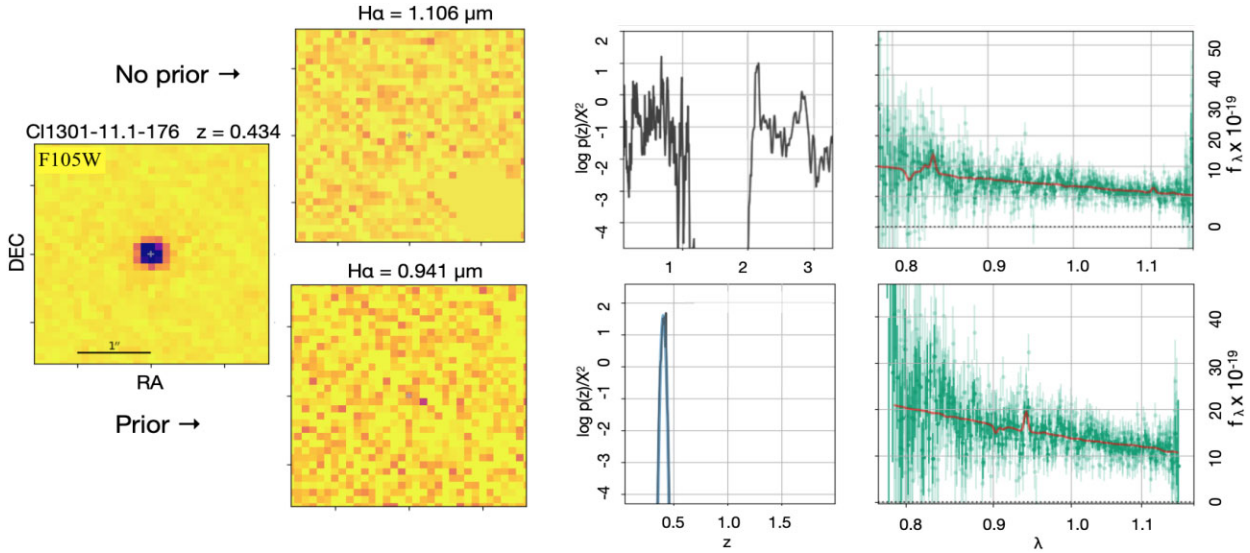

Figure 3. This collection of data products represents a comparison between the same galaxy with a blind GRIZLI extraction (top row) and with an LDP prior (bottom row). Initially, GRIZLI measured the Hα flux with $S/N = 2.99$ at $z = 0.685$. With the redshift prior, the redshift changed by 0.25 to $z = 0.434$ with the resultant the Hα flux having $S/N = 3.99$. The $F105W$ direct image of the stellar content is on the far left, followed by the detected Hα emission-line map. In the third panel is the $p(z)$ from the redshift fitting algorithm (black line), with a blue line indicating the applied Gaussian redshift prior in the bottom panel. The $p(z)$ after the prior is applied (black line – bottom row, middle panel) is much more constrained than the blind $p(z)$. Note the redshift scale differences between the extractions. The rightmost panel shows the 1D spectra in green with a fit (red). The blind extraction for the $p(z)$ is very uncertain and could easily be a high- or low-z galaxy. The application of the prior dramatically alters the results of the redshift determination. The ability of the prior to be successfully applied to a low S/N Hα galaxy is important towards creating a sample that is not biased towards strong Hα line galaxies.

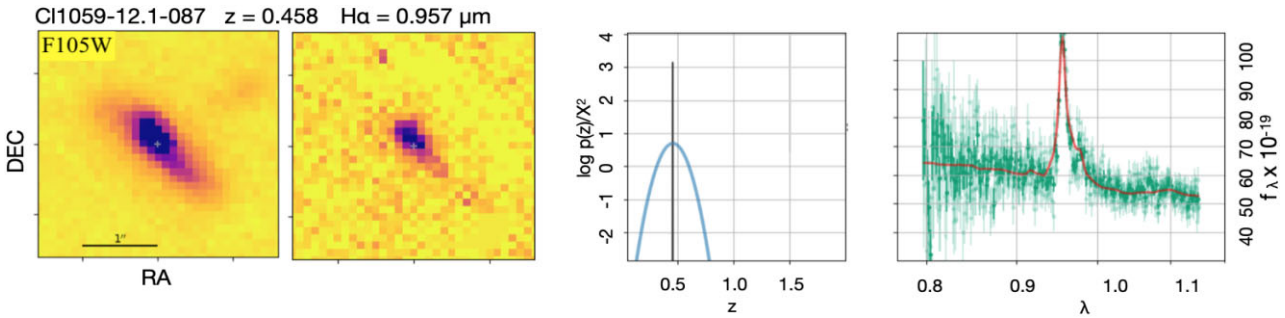

Figure 4. (Two left-hand panels): RA and Dec. postage stamps show the stellar continuum from the $F105W$ 1.05 μm direct image and the Hα emission extraction at 0.957 μm. (Two right-hand panels): The fitted redshift, shown as the black line, is fully consistent with the photometric redshift prior probability distribution in blue. The 1D spectrum data are shown in green, with a best-fitting template in red. Note the prominent Hα emission line at 0.95 μm with an S/N of 36.6. Note that is one of the brightest Hα emission lines from our sample.

GRIZLI outputs a line flux but there are several intrinsic properties that need to be accounted for while calculating an SFR. Following the prescription in Carleton et al. (2020), a series of corrections are applied to achieve a correct Hα-based SFR. The resolution of the grism is not fine enough to distinguish between the Hα and [N II] line doublet emission, indicating that measured line fluxes include the contribution of [N II] and therefore need to be reduced to account for the additional flux. Strom et al. (2017) find that the [N II] contribution is uniform across SFR per given stellar mass, so Carleton et al. (2020) calculate this reduction through a mass-dependent metallicity relation. The mass–metallicity relation is derived from Zahid et al. (2014), which is then transformed into an Hα/[N II] ratio (Kewley & Ellison 2008), resulting in a flux reduction of $\sim$ 33 per cent for our sample. Carleton et al. (2020) required a $\sim$ 25 per cent correction for $z \sim 1$ galaxies, while 3D-*HST* (Wuyts et al. 2011) found $\sim$ 20 per cent. There is a secondary dependence of the metallicity on the SFR at a fixed stellar mass known as the fundamental metallicity relation (FMR; Mannucci et al. 2010). We used the FMR to determine how much the metallicity correction changes over the range of SFRs in our sample. As we discuss in Section 3.2, our mass-complete galaxies range in $\log_{10}$(SFR) from -0.5 to 0.5. At $\log_{10}(M_*) = 10.0$, the FMR predicts that log(O/H) changes from 8.82 to 8.98. In comparison, at $\log_{10}$(SFR) $= 0$, the FMR predicts that log(O/H) changes from 8.8 to 9.07 over the full mass range of our mass-complete sample $\log_{10}(M_*) = 9.7$ to 11. While the mass dependence of the metallicity dominates over the residual dependence on the SFR, the dependence on the SFR is not negligible. This implies that we may be underestimating the uncertainty in this correction. However, [N II]/Hα saturates at high metallicity, which should minimize the effect of this residual SFR dependence on our results.

The Hα line is also contaminated with emission from post-asymptotic giant branch (AGB) stars and this is remedied by subtracting $f_{\rm AGB} = 2 \times 1.37 \times 10^{29}$ erg s^{-1} M$_\odot^{-1}$ from the line

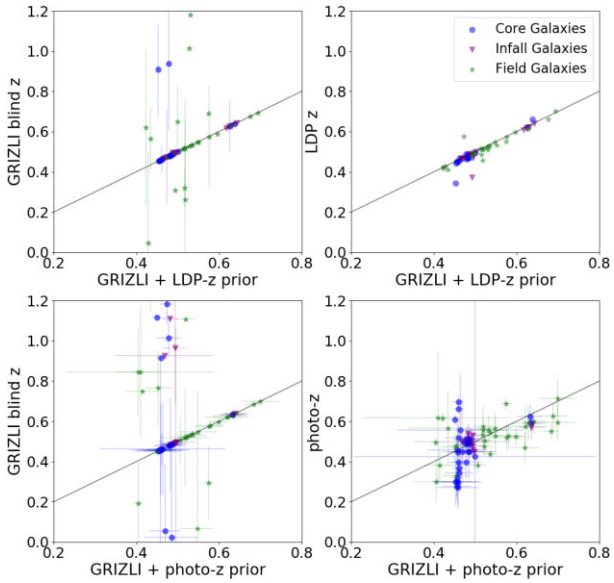

Figure 5. The GRIZLI-extracted redshift (no prior) versus the GRIZLI-extracted redshift with an applied spectroscopic (top left) or photometric (bottom left) prior for cluster core (blue circle), infall (purple triangle), and field (green star) galaxies. A majority of objects fall along the 1-to-1 line in black, indicating that the GRIZLI extractions without a prior can be reliable. The galaxies significantly above 1-to-1 line in the top and bottom left originate from a single pointing with a significantly higher background, and hence poor blind GRIZLI redshifts. These galaxies are mostly corrected with the LDP spectroscopic or photometric redshift prior. Several low S/N Hα galaxies are also corrected through the prior. The 68 per cent confidence levels for the photometric, GRIZLI blind and GRIZLI + photometric redshifts are shown with error bars, while the errorbars on the LDP or GRIZLI + LDP redshifts are too small to be visible. This photometric relation has noticeably more scatter around the 1-to-1 line, which is a reflection of the reduced accuracy of photo-z measurements. The GRIZLI-extracted redshifts with a spectroscopic (top right) or photometric (bottom right) prior are shown in comparison to their blind redshift.

luminosity (Carleton et al. 2020), where the factor of two comes from the 1:1 ratio of [N II]/Hα lines (Belfiore et al. 2016) and the 1.37×10^{29} factor comes from the expected contribution of ionization by the post-AGB stars. When compared to the Hα line luminosity ($\sim 10^{40}$–10^{42}), the post-AGB emission is negligible. This correction is equivalent to a reduction in the specific SFR of 1.2×10^{-12} yr^{-1}.

Dust within each galaxy is responsible for the extinction and scattering of light and thus, contributes towards suppressed Hα emission lines and SFRs. We correct for Hα attenuation following the approach from Wuyts et al. (2013), who relate the attentuation at Hα ($A_{\mathrm{H}\alpha}$) to that in the continuum at 6563 Å ($A_{6563\,\text{Å}}$) using the relation $A_{\mathrm{H}\alpha} = 1.9A_{6563\,\text{Å}}$–$0.15A^2_{6563\,\text{Å}}$. As demonstrated in Carleton et al. (2020) using Balmer decrements from the LEGA-C survey (van der Wel et al. 2016), the Wuyts et al. (2013) approach yields line attenuations within 0.32 mag of the Balmer-decrement approach, with a 1.2 mag scatter and no dependence of the disagreement on the measured extinction.

Given the limited spectral coverage of the G102 grism and the issues with our SED calibration discussed earlier in the text, we cannot compute $A_{6563\,\text{Å}}$ directly for each galaxy. Instead, we develop a method to derive a statistical attenuation correction in which we determine the dependence of $A_{6563\,\text{Å}}$ on *UVJ* colour for a sample of galaxies from UltraVISTA which have extremely well-characterized SEDs and redshifts (Muzzin et al. 2013). We use a subset of ULTRAVISTA galaxies with a similar redshift and stellar mass distribution to our own and fit their SEDs using MAGPHYS (da Cunha, Charlot & Elbaz 2008), which is a Bayesian SED fitting code that deals with attenuation both from birth clouds and from diffuse dust. Neither of these is a good approximation for the total attenuation used in the Wuyts et al. (2013) formula used above. We therefore derive the effective total continuum extinction by taking the ratio of the attenuated and unattenuated model for each galaxy at 6563 Å, where the attenuated model folds in the distinct attenuation sources for the different stellar populations. We then derive the optical depth at 6563 Å $\tau_{6563\text{Å}} = -\ln(10^{\log I_{\mathrm{att}}}/10^{\log I_{\mathrm{o}}})$, where $\log_{\mathrm{att}}$ is the flux of the attenuated SED and $\log_{\mathrm{o}}$ is the unattenuated SED curve. We compute the attenuation in magnitudes as $A_{6563\,\text{Å}} = 1.086 \times \tau_{6563\,\text{Å}}$.

We then compute the median ULTRAVISTA attenuation in 0.2 mag bins of *UVJ* colour space and apply to each EDisCS galaxy the attenuation corresponding to the appropriate *UVJ* colour cell (Fig. C1). This final correction for $A_{\mathrm{H}\alpha}$ is folded into the Hα SFR, which is calculated from Kennicutt & Evans (2012) as

$$\log_{10}\left(\mathrm{SFR}_{\mathrm{H}\alpha}/\mathrm{M}_\odot\,\mathrm{yr}^{-1}\right) = \log_{10}(L_{\mathrm{H}\alpha}/\mathrm{L}_\odot) - 41.27 + 0.4A_{\mathrm{H}\alpha}, \quad (4)$$

where

$$L_{\mathrm{H}\alpha}(\mathrm{L}_\odot) = 4\pi f_{\mathrm{H}\alpha} D_{\mathrm{L}}^2 - 2 \times 1.37 \times 10^{29}\,\mathrm{erg\,s^{-1}} \times \log_{10}(M_*/\mathrm{M}_\odot). \quad (5)$$

The median Hα attenuation correction is 0.48 for the mass-complete sample, and is 0.79 and 0.26 for our UVJ star-forming and quiescent galaxies, respectively.

3 RESULTS

3.1 Galaxy sample properties

From the Just et al. (2019) catalogue, there are 581 EDisCS galaxies in the 12 *HST* pointings FOV. This is further reduced to 326 after limiting the redshift range to $0.4 < z < 0.7$. Adopting an S/N in Hα cut > 3 results in 190 sources in the sample. Finally, removing extractions that are unsatisfactory due to poor contamination modelling, artefacts, or being on the edge of the chip result in a sample of 163 galaxies, of which 67 (30 core, 13 infall, 24 field) are above the mass-complete limit of $\log_{10}(M_*/\mathrm{M}_\odot) = 9.75$. This mass-complete sample of Hα-emitter galaxies is dominated by blue, star-forming objects as shown in the *UVJ* diagram in Fig. 6. We discuss corrections to the wide-field photometry in more detail in Appendix A.

In Fig. 7, we present the distributions of the stellar masses and redshift for each environment in the mass-complete sample. While the core and infall have similar median values for M_* (K–S statistic of 0.12), the field masses average slightly higher. However, they follow a similar distribution with a two-sample K–S statistic of 0.32 and 0.29 with the core and infall regions, respectively.

In contrast, the redshift distributions have significant differences (K–S statistics: core-infall (0.60), core-field (0.65), infall-field (0.46)), with the field having the highest median value of the three environments. We therefore correct the SFRs of field galaxies to the median redshift of the cluster sample (0.48) using the following relation from Schreiber et al. (2015):

$$\log_{10}\left(\mathrm{SFR}_{\mathrm{MS}}[\mathrm{M}_\odot\,\mathrm{yr}^{-1}]\right) = m - m_0 + a_0 r - a_1[max(0, m - m_1 - a_2 r)]^2. \quad (6)$$

Here, $r = \log_{10}(1 + z)$, where z is difference between the median and individual redshift, $m_0 = 0.5$, $a_0 = 0.15$, $a_1 = 0.3$, $m_1 = 0.6$, $a_2 = 2.5$, and $m = \log_{10}(M_*/10^9\,\mathrm{M}_\odot)$. For each galaxy in the field, we compute the difference in SFR that would be expected from

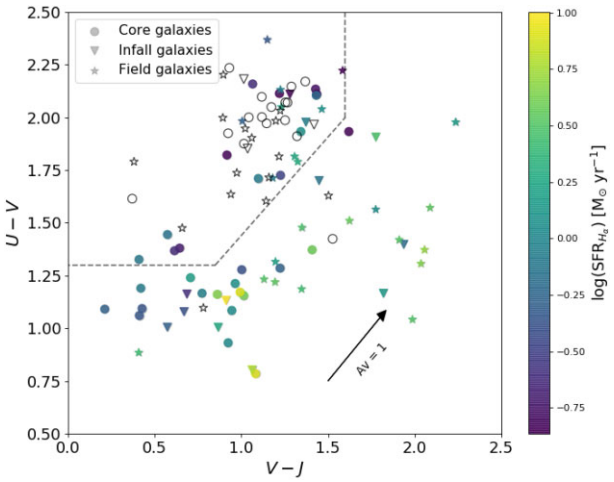

Figure 6. $U - V$ versus $V - J$ rest-frame colours colour-coded by Hα-based SFR for the mass-complete sample of *HST*-observed galaxies. Galaxies with S/N <3 in Hα are grey open symbols, which are predominantly located in the quiescent clump. The SFR colour-coded points are the final sample of 67 galaxies selected for S/N > 3 and emission line extraction quality. 51 of the 67 of the sources with F(Hα) S/N > 3 lie in the star-forming region, with 21 residing in the quiescent region. The stellar continuum and Hα emission-line maps for the 21 passively classified galaxies are shown in Appendix B1. Black dashed lines follow the quiescent and star-forming definition of Williams et al. (2009).

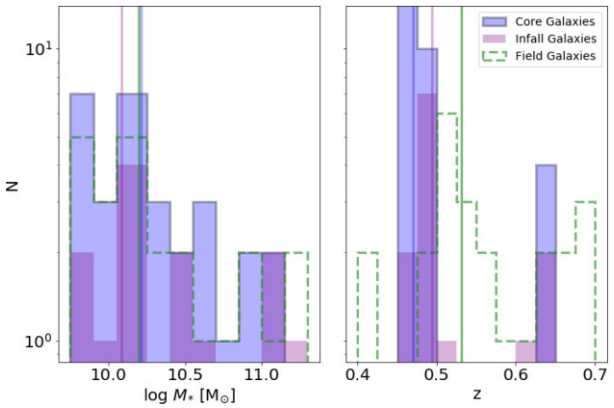

Figure 7. (Left) The distribution of the stellar masses for each of the core, infall, and field mass-complete samples is shown in the blue, purple, and green-dashed histograms. The median value for each sample is the vertical line. (Right) The same three samples are shown with their distributions in redshift space, with the median shown again as the vertical lines. A more significant difference in z is apparent between the field and cluster samples and is corrected following the equation in Section 2.6. The elevated median for the infall sample is due to the lack of two samples for Cl1059 at $z = 0.4564$, which is the lowest z cluster. Thus, the median z is offset to a higher value than the core which includes galaxies from this cluster.

equation (6) between the galaxy and median redshift. We apply that difference to correct the SFRs to the median redshift. This allows us to correct for any variation in the SFR that comes from redshift evolution. The lack of an infall sample in Cl1059 at $z = 0.4564$ is likely driving the variation in the median z's between the core and infall distributions.

3.2 Stellar mass–SFR relations

In Figs 8 and 9, we present the Hα-derived SFR–M_* main-sequence relation and specific SFR for four EDisCS clusters separated into three environments: core (blue circles), infall (purple triangles), and field (green stars) for 163 galaxies in the left-hand panel. In the right-hand panel, galaxies are divided by their classification from Fig. 6, where red triangles are defined as *UVJ*-quiescent. Both panels include galaxies with S/N in Hα < 3 as down arrows at their 3σ upper limit SFR. A scatter of ∼1 dex is observed across all masses with a lack of flattening of the SFR relation for more massive galaxies in the cluster core as shown with Schreiber et al. (2015). The median $\log_{10}$(SFR) for the mass-complete sample with S/N > 3 in Hα is 0.25 with a standard deviation of 0.43, while the *UVJ* star-forming sample has a median of 0.46 and standard deviation of 0.37. The infall times of galaxies into the cluster environment can vary and contribute towards this large scatter, which is double the 1σ value of 0.25 dex in GLASS clusters from Vulcani et al. (2016). The mean SFRs for the three EDisCS clusters in Finn et al. (2005) at $z = 0.75$ are shown as orange squares. 2D image cutouts of the stellar and Hα maps for the *UVJ* quiescent are available in Fig. B1. We also show the SFR–M_* distribution on a cluster-by-cluster basis in Fig. 10. The apparent distribution of galaxies seen in Fig. 8 is not dominated by any individual cluster but rather contains small contributions from each cluster. The distribution of SFRs appears to be similar between the clusters.

There are 21 galaxies identified as quiescent based upon the Just et al. (2019) *UVJ* rest-frame colours, with five of them being in the core, two in the infall, and nine in the field. These are identified as red triangles in the right-hand panel of Fig. 8. As seen in Fig. 6, there are galaxies that are quiescent based on their *UVJ* colours but which have significant Hα emission. We will discuss these galaxies in Section 4. GRIZLI produces a stellar continuum and emission-line map for each observed galaxy, which is shown in Fig. B1 for select galaxies.

In Fig. 11, we compare our Hα SFRs to those derived from *Spitzer* MIPS 24 μm emission (Finn et al. 2010). The observations from Finn et al. (2010) only covered the central regions of the EDisCS clusters. Therefore, our comparison only involves galaxies that are either in the core or are field galaxies in the central projected area of the cluster. Many of the galaxies in our Hα sample are not detected in 24 μm. 15 galaxies (14 core and one field) in our Hα sample are detected at 24 μm and these have SFR(Hα) that are very well correlated with SFR(24 μm) but are lower by 0.2–0.3 dex. Given the median attenuation at Hα of 0.46 mag, it is reasonable to assume that we might have slightly underestimated our attenuation values towards Hα. It might also be that the 24 μm detections are biased towards galaxies with a higher-than-average amount of obscured star formation. To test the robustness of our attenuation correction, we computed an alternate correction from Kennicutt & Evans (2012) in which observed Hα is corrected for attenuation using a scale applied to the total IR luminosity (L(TIR)) such that $L(\mathrm{H}\alpha)_{\mathrm{corr}} = L(\mathrm{H}\alpha)_{\mathrm{obs}} + 0.0024L(\mathrm{TIR})$. L(TIR) was determined in Finn et al. (2010) using Chary & Elbaz (2001) to scale the observed 24 μm flux to L(TIR). The SFR derived from this alternatively corrected Hα luminosity is very close to our default value, with a median difference of only 0.13 dex and a scatter of 0.17 dex. These comparisons give us confidence that our *UVJ*-derived attenuation is comparable to that derived using IR estimates. As a final note, in Appendix D1, we show a comparison of the main sequence from different authors at the same redshift. These estimates use both Hα and UV + IR SFR indicators and also differ by ∼0.3 dex. This underscores the systematic uncertainty inherent when comparing different SFR indicators. As an alternative way of comparing the SFRs across

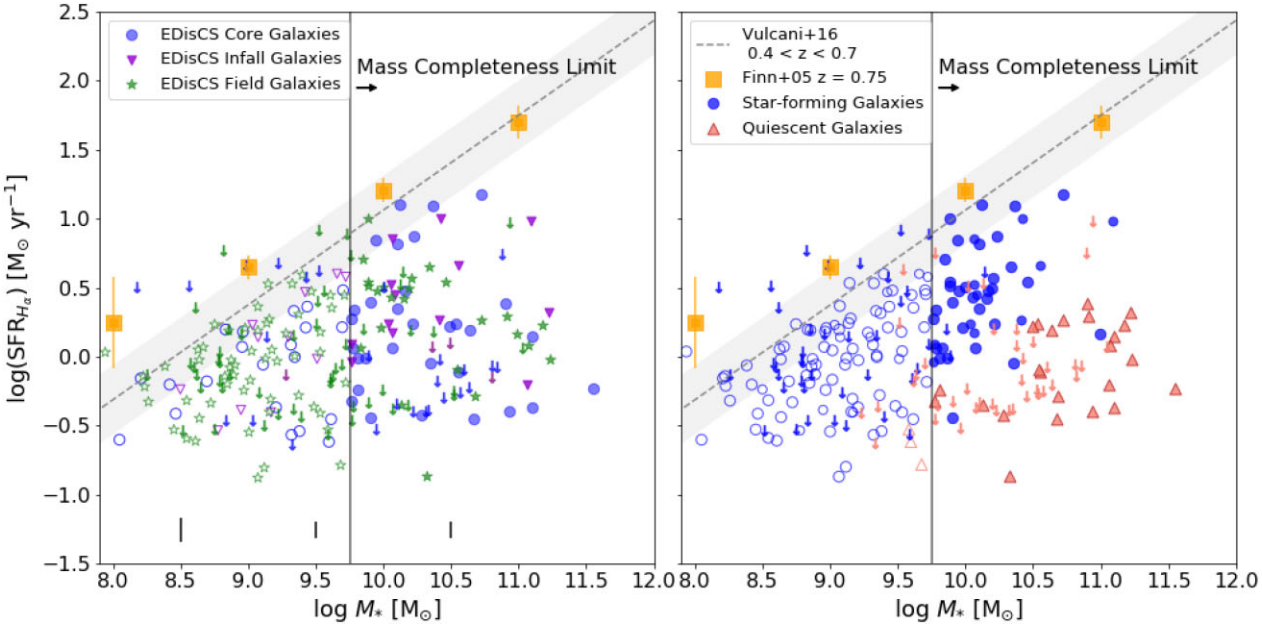

Figure 8. The H α-based SFR–M_* main-sequence relation for 163 S/N >3 and 82 S/N <3 (down arrow) galaxies. (Left) The locations of these galaxies are distributed among the cluster core (blue circles), infall region (purple triangles), and field samples (green stars), where the mass-completeness line is denoted by the vertical black line and filled in symbols and with median errors shown as black lines in three mass bins for all environments at the bottom of the plot. The <3 S/N galaxies are plotted at their 3σ limit, which occupy the lowest SFRs of the main sequence here. These data are systematically above the main-sequence relations defined by Whitaker et al. (2012) and Schreiber et al. (2015), which is shown in Appendix D. The scatter is larger than the literature but is still expected due to varying SFHs and other disturbances throughout a galaxy lifetime. A comparison is shown to the EDisCS narrow-band H α SFRs in Finn et al. (2005) (orange squares) at $z = 0.75$ and H α SFRs Vulcani et al. (2016) from the GLASS clusters at $0.4 < z < 0.7$ (grey dashed line + 1σ scatter). The median statistical error in the SFR in three mass bins is shown at the bottom of the figure. (Right) This same sample is now colour-coded by location in Fig. 6, where blue circles are star-forming and salmon triangles are quiescent. The quiescent galaxies mostly occupy the lower portion of the main sequence, which also have suppressed SFRs.

environment, in Fig. 12 we show the distribution of the SFR with respect to the cluster-based main sequence from Vulcani et al. (2016) for each of the three environments in the mass-complete sample. The median SFR for each environment is ∼1 dex below the relation from Vulcani et al. (2016). While this offset may indicate problems with our extinction correction, we showed above that our H α based SFR measurements are within 0.2–0.3 dex of those based on the IR. We also demonstrate the systematic offsets in SFR estimates among different authors and attribute part of our disagreement with Vulcani et al. (2016) to this difference. We performed two-sample K–S tests on the mass-complete sample comparing core, infall, and field galaxies for all galaxies, *UVJ* star-forming galaxies, and quiescent galaxies. In all cases, the K–S probabilities were significantly larger than 0.05. Therefore, we cannot rule out the null hypothesis that the core, infall, and field galaxies are drawn from the same SFR distribution.

In Fig. 13, we plot the SFR result as a function of distance from the cluster centre in relation to R_{200}, where the mass-complete cluster sample ($>10^{9.75}$ M$_\odot$) is represented as the blue stars and the field galaxies are shown in green as a median SFR. Cluster galaxies below the mass-complete limit are plotted as grey down arrows at the 3σ limit. The median for the mass complete cluster member sample in the core and infall region is shown as a purple triangle with 1σ bootstrap resampling error bars. There is no observable difference in the SFRs between the three environments as in Fig. 8.

4 DISCUSSION

In this study, there is no significant difference in the distribution of SFRs between environments. The EDisCS cluster galaxies are roughly aligned with the GLASS clusters H α-SFR main-sequence relation, which also does not reveal a variation from the field SFRs (Vulcani et al. 2016). Koyama et al. (2013) find a similar result with H α observations of clusters but the SFR limits are not deep enough to detect significantly suppressed galaxies. However, the lack of an environmental dependence on the SFR that is normally seen across all masses contradicts the notion that dense environments are contributing or directly responsible for gas quenching as evidenced by the buildup of quiescent galaxies (Patel et al. 2009; Vulcani et al. 2010; Paccagnella et al. 2016). Indeed, the cores (Poggianti et al. 2006) and infall regions (Cooper et al., in preparation) of the EDisCS clusters have a higher quenched fraction than the co-eval field, indicating that our clusters and their environments host processes that suppress galaxy star formation.

The lack of a dependence of the SFR on environment that we find here can potentially be explained in the following ways. First, our sensitivity limits are not low enough to detect galaxies with significantly suppressed SFRs. This is evident in Fig. 8 in that the majority of the <3 S/N galaxies appear to populate the bottom of the main sequence. Thus, there may be a tail of galaxies to lower SFRs but we would be unable to detect this population with our data. The importance of highly sensitive SFR limits to interpret the distribution of SFRs in dense environments is illustrated in Vulcani et al. (2010), in which they do find an excess of galaxies in EDisCS clusters with low SFRs compared to those in the field but only because they probe well below the main sequence.

It is also possible that the galaxies within our sample have not experienced significant quenching and the reasons for this vary by environment. Within the core, galaxies may have been recently accreted and are still within the 'delay' period of the quenching

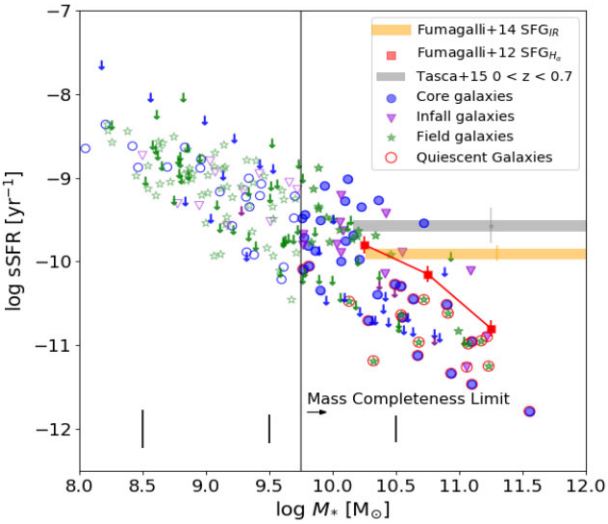

Figure 9. The Hα-based sSFR–M_* relation for 163 S/N >3 and 82 S/N <3 (down arrow) galaxies, with median errors shown as black lines in three mass bins for all environments at the bottom of the plot. The environmental locations of these galaxies are distributed among the cluster core (blue circles), infall region (purple triangles), and field samples (green stars), where the mass-completeness line is denoted by the vertical black line and filled in symbols. The <3 S/N galaxies are plotted at their 3σ limit, which occupy the lowest SFRs of the main sequence here. Comparisons to Tasca et al. (2015) at $0 < z < 0{,}7$, 3DHST (Fumagalli et al. 2012) at $z \sim 0.9$, and Fumagalli et al. (2014) at $0.3 < z < 0.7$ are shown as a grey bar, red square, and orange bar, respectively. Note that we have very few star-forming galaxies in the mass range as the comparison sets, but the Fumagalli et al. (2012) Hα field relation aligns well with our sample, though at slightly higher sSFR. The *UVJ*-quiescent galaxies, which are designated by red circles, mostly occupy the lower right portion of the relation. The statistical error of the sSFR in three mass bins is shown at the bottom of the figure for each environment.

process. In the infall region, the local density is lower than that of the core and may not create conditions capable of quenching.

Thirdly, the lack of a difference in field versus cluster SFRs could mean that the time-scale for the truncation of SF is rapid. In this case, galaxies that are undergoing external quenching will fall below our detection limits before we can observe them in their reduced SFR state. Such a rapid decline in SFRs caused by dense environments is consistent with the excess of post-starburst galaxies in dense environments as seen by Poggianti et al. (2008), Muzzin et al. (2012), and Wild et al. (2016). It is not immediately clear why there is a diversity in the distribution of SFRs in different environments among different published works. It may be that much of the 'action' is in the tails of the distribution, which requires not only deep observations, but also large sample sizes to characterize the distribution shapes well away from the median. Observations with the *James Webb Space Telescope* or deep UV + IR observations with *WISE* in the local Universe may satisfy this criteria.

We should also consider that our cluster core and infall samples could likely contain interlopers, which has been estimated to be 15 per cent or more for clusters with historical data sets (Duarte & Mamon 2015; Wojtak et al. 2018). These galaxies may appear to be spectroscopic members by superposition or our redshift determination is incorrect.

Finally, some of our clusters have significant substructure, e.g. Cl1138.2-1133 (De Lucia et al. 2009), which may make clustercentric radius a poor proxy for environment. As a result, a given range in clustercentric radius could contain a large variation in local density, and in fact does for some of our clusters (Just et al. 2019). As locally dense regions host higher quenched fractions (Patel et al. 2009; Just et al. 2019), this variation in local density could translate directly to a variation in the quenching efficiency at a fixed clustercentric radius.

4.1 *UVJ*-quiescent galaxies with Hα emission

There are 21 galaxies in the *UVJ* quiescent region that have Hα emission that is detected with S/N >3 (Fig. 6). These galaxies lie systematically closer to the dividing line between quiescent and star-forming galaxies than the rest of *UVJ* quiescent galaxies, however, they still exist at red colours consistent with the larger passive population. As can be seen in Fig. 8, these *UVJ*-quiescent Hα emitters also have systematically lower SFRs than *UVJ*-SF galaxies of the same stellar mass, and none have SFR greater than 3 M$_\odot$ yr^{-1}. The extend to SFR as low as 0.3 M$_\odot$ yr^{-1}. Continuum and emission-line postage stamps for all these galaxies are shown in Fig. B1. The emission is faint but visible in all 2D stamps and in the 1D spectrum and the spectra are free of artefacts. We entertain four possibilities to explain these sources.

First, we must explore the possibility that our rest-frame colours are uncertain and that these nominally *UVJ*-quiescent galaxies with Hα emission actually lie in the SF region but were moved into the quiescent *UVJ* region by random and systematic rest-frame colour errors. This is a potential concern, especially given the calibration challenges that we experienced with the wide-field data and the additional rest-frame colour corrections described in Appendix A. We test for this possibility by comparing the *UVJ* colours as derived from the photometry in this paper with the *UVJ* colours derived from the original EDisCS photometry in the cluster cores. The original EDisCS photometry is well calibrated and results in a very well defined passive clump at the correct colour location. We verified that the *UVJ* colours derived from the wide-field data are slightly different from the EDisCS *UVJ* colours on a galaxy-by-galaxy basis but that the differences are not significant enough to move galaxies in and out of the passive region. Therefore, we conclude that these galaxies are indeed in the *UVJ*-quiescent region and that we should discuss the implication of them having significant amounts of Hα emission.

Second, it is possible that weak active galactic nuclei (AGNs) may be contributing to some of the emission. With our data we cannot explicitly rule out the role of an AGN. Martini, Sivakoff & Mulchaey (2009) found only two X-ray AGNs in 17 clusters at $z < 0.4$. There are some objects that have spatially compact and linearly extended residuals in the emission-line maps in Fig. B1, e.g. Cl1059-12.2-447, Cl1227-11.2-259. This could be an indicator that the continuum shape is not well modelled by the GRIZLI continuum subtraction, which could occur if the continuum has significant non-stellar contributions from an AGN as such templates are not included in the GRIZLI continuum models. While this is a possibility, the emission lines for these galaxies, which admittedly have low signal-to-noise ratio, do not look broad in the 1D spectra. We examine the position in the SFR–M_* plane of the 11 objects with such linear residuals and find that they do not occupy any favoured place in either stellar mass or SFR, being sparsely spread in both quantities and not preferentially biasing the main sequence in any parameter. If these linear features do indeed correspond to AGN, the lack of bias with respect to the SFR–M_* plan would indicate that contamination by AGN is a minor contributor to the Hα flux in this population.

Third, it is possible that the Hα emission comes from a 'LIER'-like phenomena (Sarzi et al. 2006; Singh et al. 2013; Belfiore et al. 2016; Rudnick et al. 2017) in which gas from mass-loss

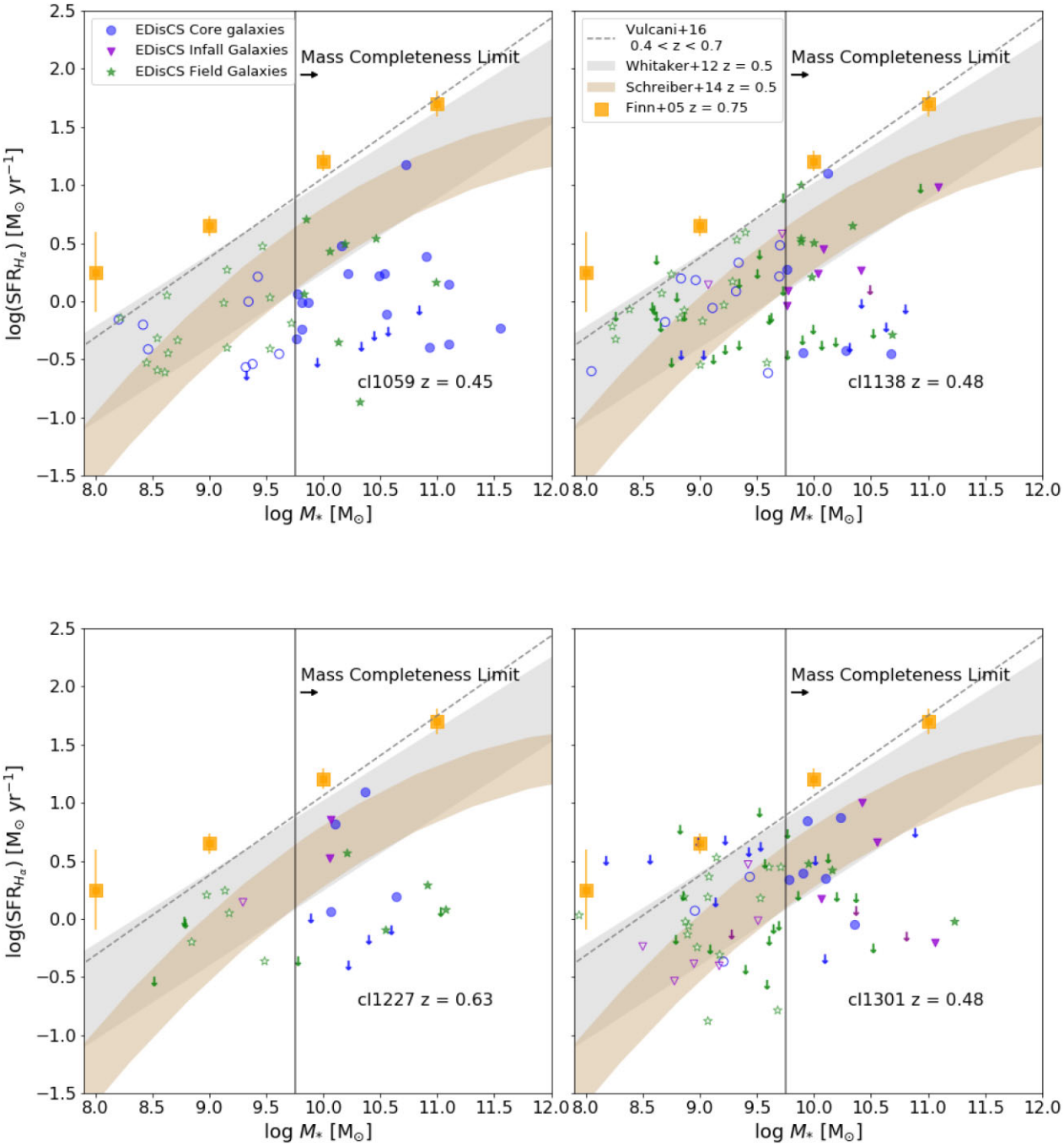

Figure 10. Each panel shows the SFR versus stellar mass as in the left-hand panel of Fig. 8 but separated by cluster. Each cluster reveals a similar distribution of galaxies below the Vulcani et al. (2016) mean distribution. This is confirmed with a two-sample K–S test for each individual cluster compared to all cluster galaxies as follows (p-value, statistic): 1059: (0.31, 0.27) 1138: (0.82, 0.20) 1227: (0.3. 0.34) 1301: (0.32, 0.31). This indicates that no cluster is offset with respect to the others and influencing the combined relation. The highest-z cluster in the bottom right, Cl1227, has noticeably fewer galaxies, which is also evident in Fig. 1. Comparison lines to Whitaker et al. (2012) and Schreiber et al. (2015) at $z = 0.5$ are shown as the grey and tan curves, respectively. The full sample in a single panel compared to Vulcani et al. (2016), Whitaker et al. (2012), and Schreiber et al. (2015) is available in Appendix D.

and accretion in quiescent galaxies are being heated by pre-existing stellar populations, mostly post-AGB stars. 'LIER' stands for 'low-ionization emission-line region', which occurs in passive galaxies that have an emission line, much like the subset of *UVJ*-passive galaxies with H α emission. In a similar emission-line study, Rudnick et al. (2017) showed that [O II] emission in EDisCS quiescent galaxies was less common in galaxies in the EDisCS clusters and groups than in the field, where quiescent [O II] emitters comprised ~ 5 per cent of the quiescent population with $M_* > 10.4$ in clusters and groups, and 30 per cent in the field. Those authors attributed this suppression of [O II] in clusters to a combination of hydrodynamic stripping and a cutoff of gas accretion in dense environments. We do not have enough galaxies in this EDisCS subsample to make the same comparison but this could be a similar population of red emission-line galaxies.

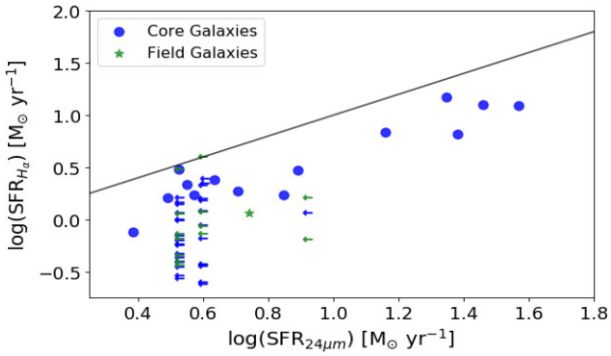

Figure 11. The MIPS 24 μm SFRs derived from the EDisCS core pointings of this sample from Finn et al. (2010) compared to the Hα SFRs in this study. There are only matches between the core (blue circle) and field (green star) because these *Spitzer* pointings did not extend to the infall region. Left arrows are non-detections in 24 μm at the 80 per cent completeness limit. The ∼0.2–0.4 dex offset from the 24 μm SFRs is similar to the one seen with GLASS.

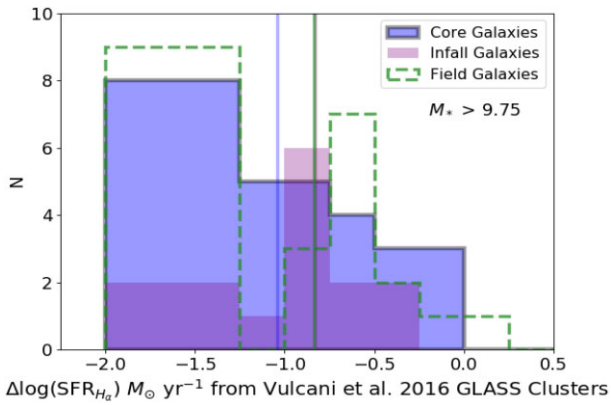

Figure 12. The difference in SFR for each of the three environments (blue = core, purple = infall, field = green) from the Vulcani et al. (2016) GLASS clusters Hα main sequence. The median values for each environment are signified by the corresponding vertical line, which are ∼1 dex below the GLASS relation.

The fourth possibility is that we are catching galaxies as they are in the process of quenching their star formation and moving from the star-forming to quiescent region. In this case, the low SFRs and position closer to the boundary of the *UVJ*-quiescent region could indicate that these galaxies are leaving the main sequence and joining the population with much lower SFRs (Cantale et al. 2016; Foltz et al. 2018; Belli, Newman & Ellis 2019; Carnall et al. 2020). Such red emission-line galaxies may be similar to those seen in other works (Wolf et al. 2009; Vulcani et al. 2010; Koyama et al. 2011) and could represent a distinct phase in the quenching of galaxies. These results imply that caution must be taken in interpreting the true quiescent nature of galaxies classified by *UVJ* techniques as truly quiescent. To assess if these *UVJ*-quiescent Hα emitters are truly quenching, it would be beneficial to obtain high signal-to-noise spectra at medium resolution to model the spectra and search for evidence of young stellar populations (Webb et al. 2020). We could also obtain deep molecular gas observations to probe the cold gas reservoirs that would be needed to power the observed star formation.

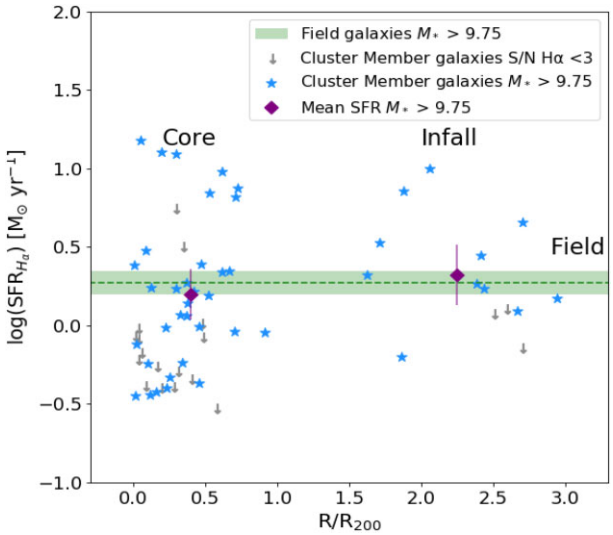

Figure 13. The distance from the centre of the cluster (defined as the BCG in White et al. 2005) is computed for each core and infall galaxy and compared to the SFR. The mass-complete sample is shown as blue stars for cluster members and the average for the field is the dashed green line, where error bars on the median are the 1σ confidence level from a bootstrap resampling. Galaxies with S/N in Hα < 3 are the grey arrows and are not accounted for in the median values. All but three of these upper limits are for *UVJ* quiescent galaxies and so the apparent radial dependence in the fraction of galaxies with upper limits just reflects the well-known radial dependence in the quiescent fraction in clusters. For the robust Hα detections, no significant radial trend exists for the mass-complete sample.

5 CONCLUSIONS AND FUTURE WORK

In this paper, we explore the environmental dependence of spectroscopically derived Hα star formation in three distinct regimes in the vicinity of four galaxy clusters at $0.4 < z < 0.7$: cluster cores, infall regions, and the field. We combine *HST*/WFC3 G102 grism observations at 1 μm with photometric and spectroscopic redshift priors to obtain a sample of 67 galaxies with secure redshifts, S/N in Hα > 3 and which are above our mass completeness limit for star-forming galaxies of $M_* > 10^{9.75}$.

Our main findings are summarized as the following points:

(i) With the combination of grism and redshift priors, we can obtain precise and accurate redshifts for galaxies with a range of stellar masses and intracluster locations.

(ii) We find no difference in the distribution of SFRs for galaxies in the three environments or as a function of radius from the cluster out to $3R_{200}$.

(iii) We find 21 galaxies that are identified as *UVJ*-quiescent galaxies but which have significant amounts of Hα emission. We explore possible explanations for this emission that include star formation in quenching galaxies, AGN, and excitation of the gas by post-AGB stars. We conclude that there may be contributions from all of these scenarios.

(iv) The similarity of the SFR distributions for our core, infall, and field samples may be attributed to the delayed-then-rapid quenching scenario, where galaxies are unaffected for the first 2–4 Gyr that they reside in the cluster environment, followed by a rapid quenching event that leaves the distribution of SFRs for star-forming galaxies unaffected. We cannot conclusively test this scenario without significantly more galaxies measured to lower SFR sensitivity limits. However, it is possible that our Hα-detected galaxies have not

experienced significant quenching processes. For the infall galaxies, this can be because of the relatively low densities that they inhabit while for the core galaxies it may be that they have recently been accreted by the cluster and are still in the 'delay' phase of their eventual quenching. Whichever intrinsic and extrinsic processes that do affect star formation in the infall regions and cores of our clusters must do so in a way that preserves the indistinguishable distribution of SFRs in the different environments, at least at the level constrained by our data.

One possibility for using this data set to explore the effect of environment on the star formation properties of galaxies would be to analyse the relative size of the stellar (traced by $F105W$) and H α discs. As different processes may result in a different ratio of these sizes, this may provide a new constraint on the quenching process. We will explore this in a future work.

ACKNOWLEDGEMENTS

GR acknowledges support from the National Science Foundation grants AST-1517815, AST-1716690 and NASA *Hubble Space Telescope* grant HST-GO-12945.001. GR also acknowledges the support of an European Southern Observatory visiting science fellowship. The work in this paper benefited significantly from interaction conducted as part of a team at the International Space Sciences Institute in Bern, Switzerland. JC thanks the Madison & Lila Self Graduate Fellowship at the University of Kansas for financial and professional support. YJ acknowledges financial support from CONICYT PAI (Concurso Nacional de Inserción en la Academia 2017) No. 79170132 and FONDECYT Iniciación 2018 No. 11180558. BV acknowledges financial contribution from the contract ASI-INAF n.2017-14-H.0, from the grant PRIN MIUR 2017 n.20173ML3WW_001 (PI Cimatti) and from the INAF main-stream funding programme (PI Vulcani). We thank Matthew Kirby for his assistance with producing the LDP redshifts that were used in this work.

DATA AVAILABILITY

The raw *HST* data are available through MAST (Program ID 12945). The ground-based redshift catalogue is available in Just et al. 2019 for clusters Cl11138, Cl1227, and Cl1301, while Cl1059 is available in White et al. (2005); DOI - 10.3847/1538-4357/ab44a0. Additional data on derived physical parameters are available in this paper.

REFERENCES

Abramson L. E. et al., 2018, AJ, 156, 29
Baade D. et al., 1999, Messenger, 95, 15
Balogh M. L., Morris S. L., Yee H. K. C., Carlberg R. G., Ellingson E., 1997, ApJ, 488, L75
Balogh M. L. et al., 2016, MNRAS, 456, 4364
Barro G. et al., 2014, ApJ, 791, 52
Belfiore F. et al., 2016, MNRAS, 461, 3111
Bell E. F., de Jong R. S., 2001, ApJ, 550, 212
Bell E. F. et al., 2004, ApJ, 608, 752
Belli S., Newman A. B., Ellis R. S., 2019, ApJ, 874, 17
Bouché N. et al., 2010, ApJ, 718, 1001
Bouwens R. J., Illingworth G. D., Oesch P. A., Caruana J., Holwerda B., Smit R., Wilkins S., 2015, ApJ, 811, 140
Brinchmann J., Charlot S., White S. D. M., Tremonti C., Kauffmann G., Heckman T., Brinkmann J., 2004, MNRAS, 351, 1151
Calzetti D., Armus L., Bohlin R. C., Kinney A. L., Koornneef J., Storchi-Bergmann T., 2000, ApJ, 533, 682
Cantale N. et al., 2016, A&A, 589, A82
Carleton T., Guo Y., Nayyeri H., Cooper M., Rudnick G., Whitaker K., 2020, MNRAS, 491, 2822
Carnall A. C. et al., 2020, MNRAS, 496, 695
Chabrier G., 2003, PASP, 115, 763
Chary R., Elbaz D., 2001, ApJ, 556, 562
Clowe D. et al., 2006, A&A, 451, 395
Cucciati O. et al., 2012, A&A, 539, A31
da Cunha E., Charlot S., Elbaz D., 2008, MNRAS, 388, 1595
Daddi E. et al., 2007, ApJ, 670, 156
De Lucia G. et al., 2004, ApJ, 610, L77
De Lucia G., Poggianti B. M., Halliday C., Milvang-Jensen B., Noll S., Smail I., Zaritsky D., 2009, MNRAS, 400, 68
De Lucia G., Weinmann S., Poggianti B. M., Aragón-Salamanca A., Zaritsky D., 2012, MNRAS, 423, 1277
Desai V. et al., 2007, ApJ, 660, 1151
Domínguez Sánchez H. et al., 2014, MNRAS, 441, 2
Dressler A., 1980, ApJ, 236, 351
Duarte M., Mamon G. A., 2015, MNRAS, 453, 3848
Dutton A. A., Conroy C., van den Bosch F. C., Prada F., More S., 2010, MNRAS, 407, 2
Elbaz D. et al., 2007, A&A, 468, 33
Erfanianfar G. et al., 2016, MNRAS, 455, 2839
Finn R. A. et al., 2005, ApJ, 630, 206
Finn R. A. et al., 2010, ApJ, 720, 87
Finn R. A. et al., 2018, ApJ, 862, 149
Foltz R. et al., 2018, ApJ, 866, 136
Fossati M. et al., 2017, ApJ, 835, 153
Fumagalli M. et al., 2012, ApJ, 757, L22
Fumagalli M. et al., 2014, ApJ, 796, 35
Gómez P. L. et al., 2003, ApJ, 584, 210
Gonzalez A. H., Zaritsky D., Dalcanton J. J., Nelson A., 2001, ApJS, 137, 117
Grogin N. A. et al., 2011, ApJS, 197, 35
Haines C. P. et al., 2015, ApJ, 806, 101
Halliday C. et al., 2004, A&A, 427, 397
Hopkins P. F., Kereš D., Oñorbe J., Faucher-Giguère C.-A., Quataert E., Murray N., Bullock J. S., 2014, MNRAS, 445, 581
Jaffé Y. L. et al., 2016, MNRAS, 461, 1202
Just D. W. et al., 2019, ApJ, 885, 6
Karim A. et al., 2011, ApJ, 730, 61
Kauffmann G., White S. D. M., Heckman T. M., Ménard B., Brinchmann J., Charlot S., Tremonti C., Brinkmann J., 2004, MNRAS, 353, 713
Kennicutt R. C. Jr, 1998, ARA&A, 36, 189
Kennicutt R. C., Evans N. J., 2012, ARA&A, 50, 531
Kewley L. J., Ellison S. L., 2008, ApJ, 681, 1183
Kodama T., Balogh M. L., Smail I., Bower R. G., Nakata F., 2004, MNRAS, 354, 1103
Koyama Y., Kodama T., Nakata F., Shimasaku K., Okamura S., 2011, ApJ, 734, 66
Koyama Y. et al., 2013, MNRAS, 434, 423
Lang P. et al., 2014, ApJ, 788, 11
Larson R. B., Tinsley B. M., Caldwell C. N., 1980, ApJ, 237, 692
Lee-Brown D. B. et al., 2017, ApJ, 844, 43
Lewis I. et al., 2002, MNRAS, 334, 673
Lotz J. M. et al., 2013, ApJ, 773, 154
McGee S. L., Balogh M. L., Wilman D. J., Bower R. G., Mulchaey J. S., Parker L. C., Oemler A., 2011, MNRAS, 413, 996
Madau P., Dickinson M., 2014, ARA&A, 52, 415
Mannucci F., Cresci G., Maiolino R., Marconi A., Gnerucci A., 2010, MNRAS, 408, 2115
Martig M., Bournaud F., Teyssier R., Dekel A., 2009, ApJ, 707, 250
Martini P., Sivakoff G. R., Mulchaey J. S., 2009, ApJ, 701, 66
Milvang-Jensen B. et al., 2008, A&A, 482, 419
Momcheva I. G. et al., 2016, ApJS, 225, 27
Moran S. M., Ellis R. S., Treu T., Smith G. P., Rich R. M., Smail I., 2007, ApJ, 671, 1503
Moustakas J., Kennicutt R. C., Tremonti C. A., 2006, ApJ, 642, 775
Muzzin A. et al., 2012, ApJ, 746, 188

Muzzin A. et al., 2013, ApJS, 206, 8
Muzzin A. et al., 2014, ApJ, 796, 65
Nelson E. J. et al., 2012, ApJ, 747, L28
Newman A. B., Treu T., Ellis R. S., Sand D. J., Nipoti C., Richard J., Jullo E., 2013, ApJ, 765, 24
Noeske K. G. et al., 2007, ApJ, 660, L43
Oemler Augustus J., Dressler A., Gladders M. G., Fritz J., Poggianti B. M., Vulcani B., Abramson L., 2013, ApJ, 770, 63
Old L. J. et al., 2020, MNRAS, 493, 5987
Paccagnella A. et al., 2016, ApJ, 816, L25
Patel S. G., Holden B. P., Kelson D. D., Illingworth G. D., Franx M., 2009, ApJ, 705, L67
Patel S. G., Kelson D. D., Holden B. P., Franx M., Illingworth G. D., 2011, ApJ, 735, 53
Peng Y.-j. et al., 2010, ApJ, 721, 193
Planck Collaboration XIII, 2016, A&A, 594, A13
Poggianti B. M. et al., 2006, ApJ, 642, 188
Poggianti B. M. et al., 2008, ApJ, 684, 888
Poggianti B. M. et al., 2009, ApJ, 693, 112
Poggianti B. M. et al., 2016, AJ, 151, 78
Quilis V., Moore B., Bower R., 2000, Science, 288, 1617
Rudnick G. et al., 2009, ApJ, 700, 1559
Rudnick G. et al., 2017, ApJ, 850, 181
Saglia R. P. et al., 2010, A&A, 524, A6
Sarzi M. et al., 2006, MNRAS, 366, 1151
Schreiber C. et al., 2015, A&A, 575, A74
Simard L. et al., 2009, A&A, 508, 1141
Singh R. et al., 2013, A&A, 558, A43
Sobral D., Best P. N., Smail I., Geach J. E., Cirasuolo M., Garn T., Dalton G. B., 2011, MNRAS, 411, 675
Speagle J. S., Steinhardt C. L., Capak P. L., Silverman J. D., 2014, ApJS, 214, 15
Strom A. L., Steidel C. C., Rudie G. C., Trainor R. F., Pettini M., Reddy N. A., 2017, ApJ, 836, 164
Tacchella S., Dekel A., Carollo C. M., Ceverino D., DeGraf C., Lapiner S., Mand elker N., Primack Joel R., 2016, MNRAS, 457, 2790
Taranu D. S., Hudson M. J., Balogh M. L., Smith R. J., Power C., Oman K. A., Krane B., 2014, MNRAS, 440, 1934
Tasca L. A. M. et al., 2015, A&A, 581, A54
Taylor E. N. et al., 2011, MNRAS, 418, 1587
Tiley A. L. et al., 2020, MNRAS, 496, 649
Treu T. et al., 2015, ApJ, 812, 114
van der Wel A. et al., 2014, ApJ, 788, 28
van der Wel A. et al., 2016, ApJS, 223, 29
van Dokkum P. G. et al., 2011, ApJ, 743, L15
van Dokkum P. G. et al., 2013, ApJ, 771, L35
Vulcani B., Poggianti B. M., Finn R. A., Rudnick G., Desai V., Bamford S., 2010, ApJ, 710, L1
Vulcani B. et al., 2011a, MNRAS, 412, 246
Vulcani B. et al., 2011b, MNRAS, 413, 921
Vulcani B. et al., 2012, A&A, 544, A104
Vulcani B. et al., 2015, ApJ, 814, 161
Vulcani B. et al., 2016, ApJ, 833, 178
Vulcani B. et al., 2017, ApJ, 837, 126
Vulcani B. et al., 2018, ApJ, 866, L25
Webb K. et al., 2020, MNRAS, 498, 5317
Wetzel A. R., Tinker J. L., Conroy C., van den Bosch F. C., 2013, MNRAS, 432, 336
Whiley I. M. et al., 2008, MNRAS, 387, 1253
Whitaker K. E., van Dokkum P. G., Brammer G., Franx M., 2012, ApJ, 754, L29
Whitaker K. E. et al., 2014, ApJ, 795, 104
White S. D. M., Zaritsky D., 1992, ApJ, 394, 1
White S. D. M. et al., 2005, A&A, 444, 365
Wild V., Almaini O., Dunlop J., Simpson C., Rowlands K., Bowler R., Maltby D., McLure R., 2016, MNRAS, 463, 832
Williams R. J., Quadri R. F., Franx M., van Dokkum P., Labbé I., 2009, ApJ, 691, 1879
Wojtak R. et al., 2018, MNRAS, 481, 324
Wolf C. et al., 2009, MNRAS, 393, 1302
Wuyts S. et al., 2007, ApJ, 655, 51
Wuyts S. et al., 2011, ApJ, 738, 106
Wuyts S. et al., 2013, ApJ, 779, 135
Zahid H. J., Dima G. I., Kudritzki R.-P., Kewley L. J., Geller M. J., Hwang H. S., Silverman J. D., Kashino D., 2014, ApJ, 791, 130

SUPPORTING INFORMATION

Supplementary data are available at *MNRAS* online.

JRC_Ha_Supplementary_Tables.pdf

Please note: Oxford University Press is not responsible for the content or functionality of any supporting materials supplied by the authors. Any queries (other than missing material) should be directed to the corresponding author for the article.

APPENDIX A: COLOUR CORRECTIONS

As described in Just et al. (2019), there were multiple calibration challenges with the wide-field photometry that we use in this work, which was not taken under photometric conditions. The WFI photometry in Just et al. (2019) was calibrated to the EDisCS core photometry and a subsequent calibration step was applied to minimize the residuals of photometric versus spectroscopic redshifts. Despite this, the calibration has produced reasonably good photometric redshifts and it later became apparent that the rest-frame *UVJ* colours had additional calibration issues, likely resulting from a non-trivial by-product of the multiple zero-point calibration steps that we undertook in Just et al. (2019). While the *UVJ* colours for each cluster had a clear quiescent clump and SF sequence, they were each systematically shifted with respect to each other, and to the quiescent clump as defined from the well-calibrated EDisCS photometry on the cluster cores.

We therefore undertook an additional calibration step in which we used the median colours of quiescent galaxies in the wide-field sample and shifted the $U - V$ and $V - J$ colours such that this clump matched the median *UVJ* colours of the spectroscopically confirmed galaxies from EDisCS that had no emission lines in their spectra. Although calculated for just the quiescent galaxies, these shifts were applied to all galaxies on a cluster-by-cluster basis. These shifts were <0.2 in colour but resulted in all of our fields having well-matched *UVJ* sequences. This gives us the ability to robustly separate galaxies in different regions of *UVJ* space. The adjustment to the colours was also important for our use of the $U - V$ colour to compute stellar mass-to-light ratios and stellar masses (Section 3.1). In practice, the correction was mostly applied to the rest-frame *V*-band magnitude. The rest-frame *U*-band magnitude was derived from well-calibrated *B*-band observations and the *J*-band magnitude was calibrated well to the 2MASS photometry. The *V* magnitude was more tied to the problematic WFI photometry.

APPENDIX B: VISUAL INSPECTION OF GALAXIES WITH GRIZLI

In Fig. 6, 21 galaxies are identified as quiescent based upon the Just et al. (2019) *UVJ* rest-frame colours, with five of them being in the core, two in the infall, and nine in the field. These are identified in the right-hand side of Fig. 8 as salmon triangles. GRIZLI produces a stellar continuum and emission-line map for each observed galaxy, which is shown in Fig. B1. Many of the galaxies appear to have diffuse Hα with little-to-no stellar structure, indicating that these may be early-type galaxies.

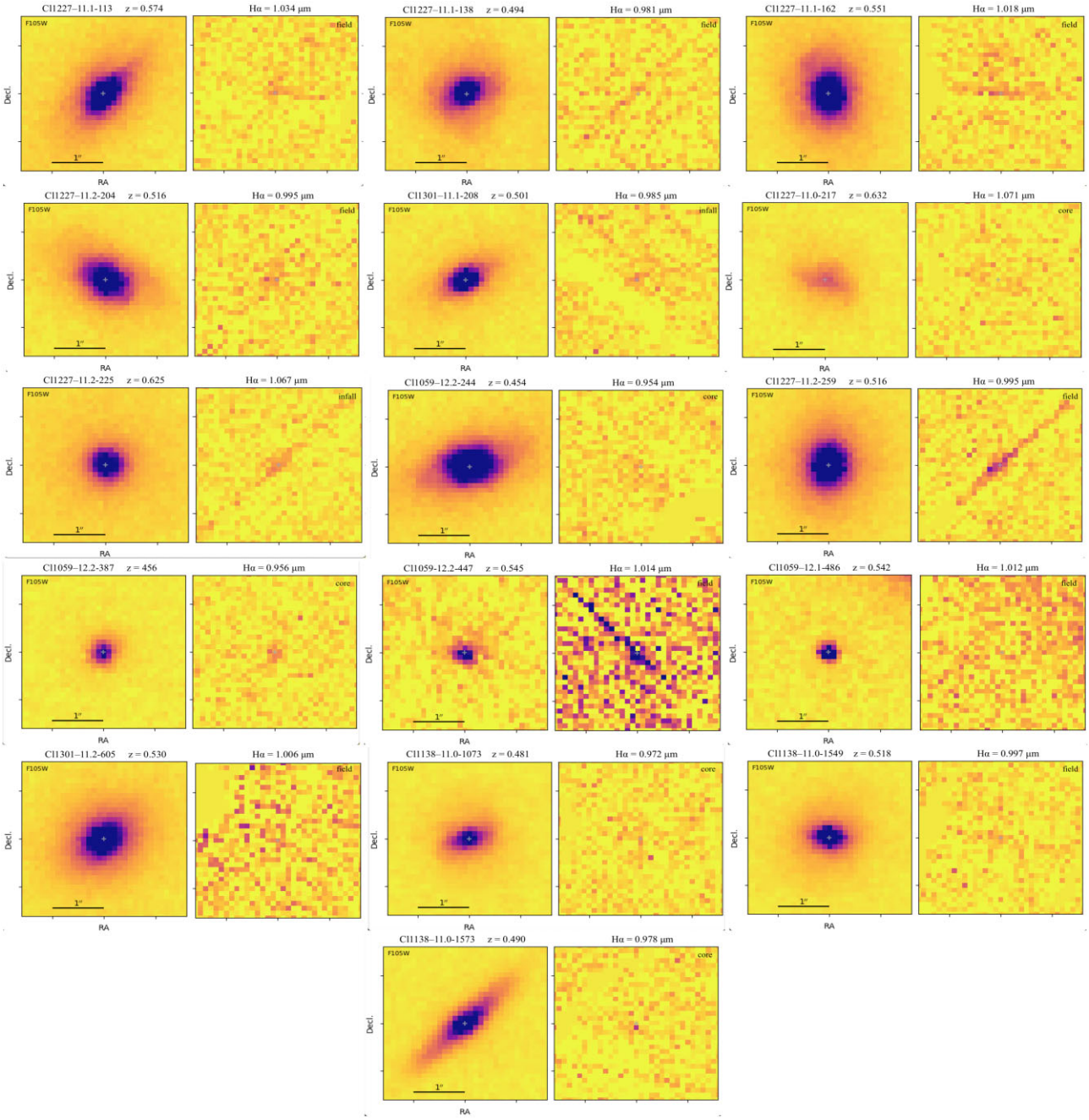

Figure B1. The stellar continuum (left) and H α line emission map (right) for each UVJ quiescent galaxy shown as a pair of images. The direct *F*105*W* images for each galaxy show signatures of early-type galaxies with a lack of spiral arms or clumpy morphology. The H α emission maps are typically low intensity or diffuse distributions, which makes inferences about the gas morphology difficult.

APPENDIX C: DERIVATION FOR EXTINCTION AT H α

The narrow spectral range of the *HST* G102 grism window does not allow us to determine the attenuation at H α from the grism data alone, and our SED calibration problems prevent us from using direct SED fits to do so. We therefore run MAGPHYS (da Cunha et al. 2008) on the ULTRAVISTA catalogue (Muzzin et al. 2013) to determine the continuum attenuation at 6563 Å. We run MAGPHYS without the UV and narrow-band filters as the SED fits were poorer using those filters. Our conclusions are unchanged if we include the UV and narrow-band filters, but the scatter of continuum attenuation increases. As described in the text, we use the ratio of the attenuated and unattenuated stellar continuum to derive the optical depth of the continuum at 6563 Å, which we convert to the attenuation in magnitudes at 6563 Å using $A_{6563\,\text{Å}} = 1.086 \times \tau_{6563\,\text{Å}}$. In Fig. C1, we show the median and interquartile range of $A_{6563\,\text{Å}}$ for the ULTRAVISTA sample. We use this distribution of $A_{6563\,\text{Å}}$ in *UVJ* space, to infer the $A_{6563\,\text{Å}}$ of our target galaxies by matching our galaxies to the nearest grid cell in *UVJ*-space. As described in the text, we then use $A_{6563\,\text{Å}}$ to derive the line attenuation at H α.

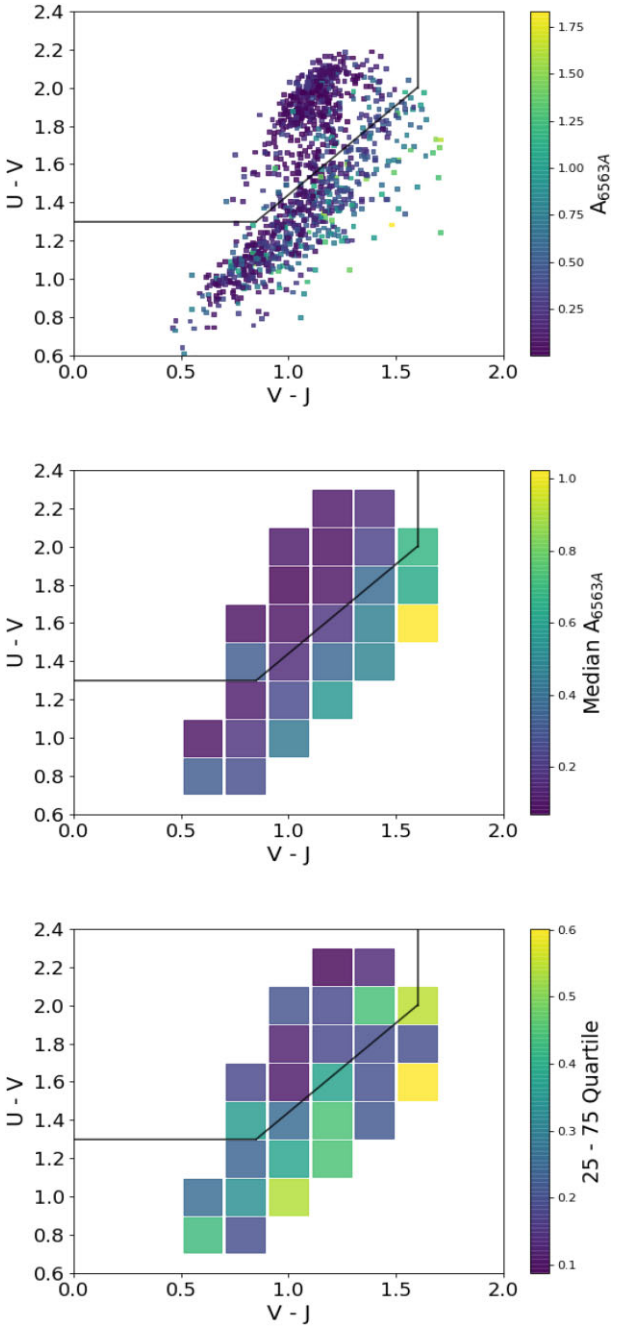

Figure C1. (Top) A *UVJ* diagram colour-coded by $A_{6563\,\text{Å}}$ is shown for a subset of the ULTRAVISTA catalogue that is similar in redshift and mass distribution to the *HST* sample in this study. (Middle) The median in 0.2 bins in $U - V$ and $V - J$ from the top plot is shown, which is used to match in colour–colour space to the *HST* sample. If a galaxy falls outside the distribution of ULTRAVISTA, it is matched to the nearest bin. *UVJ*-quiescent galaxies have low A_v as expected and redder star-forming galaxies have elevated values. (Bottom) The spread of each bin across the 75–25 per cent quartile. The spread is noticeably small in the passive region. Black lines in all plots are the Williams et al. (2009) boundaries.

APPENDIX D: MAIN-SEQUENCE COMPARISONS

In Fig. D1, we show a version of Fig. 8, but now with main-sequence determinations from Whitaker et al. (2012) and Schreiber et al. (2015) at the median redshift of 0.487 for our sample. These determinations of the main sequence use SFRs determined from UV + IR and are systematically below the H α determinations of Vulcani et al. (2010). They are consistent with the bulk of our *UVJ* star-forming galaxies, but it is worth noting that our SFRs are systematically below the IR-based SFRs of Finn et al. (2010). Taken together, this illustrates the significant systematic offsets between different SFR indicators and the importance of internal comparisons.

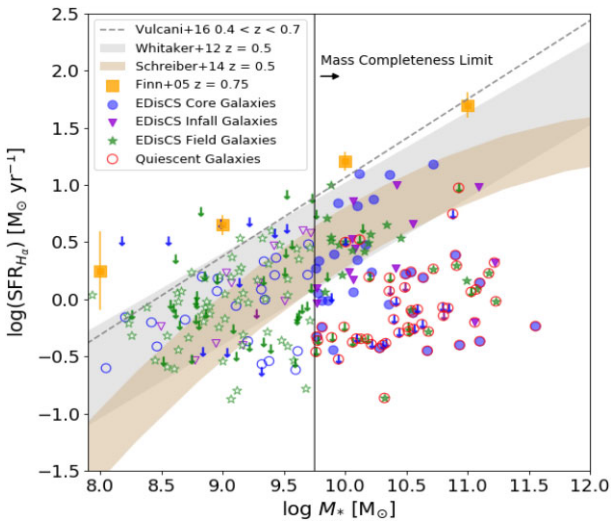

Figure D1. The main sequence for the galaxies with S/N > 3 in the core (blue circle), infall (purple triangle), and field (green stars) regions, where *UVJ* quiescent galaxies are circled in red and galaxies with less than S/N < 3 are shown as the down arrows. Galaxies with S/N < are shown at their 3σ value as down arrows with a corresponding environment colour. We show different determinations of the star-forming main sequence. As in Fig. 8, we show the cluster main-sequence relations from Vulcani et al. (2016) as a grey dashed line and Finn et al. (2005) as orange squares. We also show UV + IR-based determinations for field galaxies from Whitaker et al. (2012) in grey and Schreiber et al. (2015) in brown, both at $z = 0.5$ and with 0.3 dex scatter. The star-forming galaxies in our sample are in good agreement with both Whitaker et al. (2012) and Schreiber et al. (2015). The *UVJ*-quiescent galaxies are mostly below these relations by ∼0.5 dex.

This paper has been typeset from a TEX/LATEX file prepared by the author.